General Disclaimer

One or more of the Following Statements may affect this Document

- This document has been reproduced from the best copy furnished by the organizational source. It is being released in the interest of making available as much information as possible.

- This document may contain data, which exceeds the sheet parameters. It was furnished in this condition by the organizational source and is the best copy available.

- This document may contain tone-on-tone or color graphs, charts and/or pictures, which have been reproduced in black and white.

- This document is paginated as submitted by the original source.

- Portions of this document are not fully legible due to the historical nature of some of the material. However, it is the best reproduction available from the original submission.

NASA TECHNICAL MEMORANDUM

NASA TM-73,259

NASA TM-73,259

COMPUTATION OF THE INVISCID SUPERSONIC FLOW ABOUT CONES AT LARGE ANGLES OF ATTACK BY A FLOATING DISCONTINUITY APPROACH

James Daywitt and Paul Kutler
Ames Research Center
Moffett Field, California 94035

Dale Anderson
Iowa State University
Ames, Iowa 50011

August 1977

COMPUTATION OF THE INVISCID SUPERSONIC FLOW ABOUT CONES AT LARGE ANGLES OF ATTACK BY A FLOATING DISCONTINUITY APPROACH

James Daywitt* and Paul Kutler
NASA - Ames Research Center
Moffett Field, California 94035

and

Dale Anderson
Iowa State University
Ames, Iowa 50011

*Present address of James Daywitt: Institute for Computer Applications in Science and Engineering, NASA - Langley Research Center, Hampton, Virginia 23665

TABLE OF CONTENTS

NOMENCLATURE

a	Speed of sound
a,b,c	Least-squares coefficients for crossflow shock upstream surface pressure
$\tilde{a},\tilde{b},\tilde{c}$	Ratio of ξ_z, ξ_ϕ, and 1 to ξ_x
A,B,C	Ellipse shape parameters for initial bow shock estimate
A_3	Vector of flow variables in the nonconservation-law form of the Euler equations
$[A_1]$	θ-derivative coefficient matrix in the nonconservation-law form of the Euler equations
$[A_2]$	ϕ-derivative coefficient matrix in the nonconservation-law form of the Euler equations
b,c	Coefficients in surface total energy as a function of pressure equation
B	Parameter in meridional clustering transformation
$[\bar{B}_1]$	$\bar{X}$-derivative coefficient matrix in the discontinuity aligned nonconservation-law form of the Euler equations
$[\bar{B}_2]$	$\bar{Y}$-derivative coefficient matrix in the discontinuity aligned nonconservation-law form of the Euler equations
CN	Courant parameter
d	Vector of dependent variables in the nonconservation-law form of the Euler equations
d,e,f	Least-squares coefficients for crossflow shock downstream surface pressure
e	Total energy per unit volume
$\tilde{E}$	R-dependent vector of conservation-law variables
E'	z-dependent vector of conservation-law variables
F	X-dependent vector of conservation-law variables
$\bar{F}$	$\bar{X}$-dependent vector of conservation-law variables

$\tilde{F}$	θ-dependent vector of conservation-law variables
F'	r-dependent vector of conservation-law variables
F*	ξ-dependent vector of conservation-law variables
g,h,i	Least-squares coefficients for crossflow shock upstream surface Mach number
G	Y-dependent vector of conservation-law variables
$\bar{G}$	$\bar{Y}$-dependent vector of conservation-law variables
$\tilde{G}$	ϕ-dependent vector of conservation-law variables, spherical polar coordinate system
G'	ϕ-dependent vector of conservation-law variables, cylindrical polar coordinate system
G*	Φ-dependent vector of conservation-law variables
H	(τ,X,Y) source term vector of conservation-law variables
$\bar{H}$	$(\bar{\tau},\bar{X},\bar{Y})$ source term vector of conservation-law variables
$\tilde{H}$	(t,R,θ,ϕ) source term vector of conservation-law variables
H'	(z,r,ϕ) source term vector of conservation-law variables
H*	(Φ,ξ) source term vector of conservation-law variables
$\hat{l}_R,\hat{l}_\theta,\hat{l}_\phi$	Unit vectors in spherical polar (R,θ,ϕ) directions
$\hat{l}_z,\hat{l}_r,\hat{l}_\phi$	Unit vectors in cylindrical polar (z,r,ϕ) directions
[I]	Identity matrix
k	Nondimensionalization parameter
L	ϕ-function in Newton-Raphson iteration for $\phi_{\tilde{s}}$
min	Minimum
max	Maximum
M_{cf}	Crossflow Mach number
$\tilde{M}_{l_{rel}}$	Crossflow shock upstream normal relative Mach number
M_∞	Free-stream Mach number

$\hat{n}_c$	Unit vector normal to cone surface
$\hat{n}_{\tilde{s}}$	Unit vector normal to crossflow shock
$\tilde{n}_\theta$	θ-component of unit vector normal to crossflow shock
$\tilde{n}_\phi$	ϕ-component of unit vector normal to crossflow shock
N	Scalar in the equation for the cone surface tangent vector, $\vec{T}$
p	Pressure
$\tilde{p},\tilde{\rho},\tilde{u},\tilde{v},\tilde{w},\tilde{q}$	Surface flow variables in the corrector step following the nonisentropic Abbett scheme turn
q	Velocity modulus
$q_{\tilde{s}}$	Crossflow shock speed normal to the shock
$q_{\tilde{s}_{\bar{\tau}}}$	Crossflow shock acceleration normal to the shock
q_{vs}	Vortical singularity speed
$q_{vs_{\bar{\tau}}}$	Vortical singularity acceleration
r_c	Cone cylindrical radius
r_s	Bow shock cylindrical radius
r_{s_ϕ}	Slope of the bow shock in the ϕ-direction
R,θ,ϕ	Spherical polar coordinates
$\tilde{R}$	Terms in the crossflow shock acceleration equation
S	Entropy
t	Time
$\hat{t}_c$	Unit vector tangent to cone surface in z,r-plane
$\vec{T}$	Vector tangent to cone surface in z,r-plane
u,v,w	Velocity components in spherical polar (R,θ,ϕ) directions
u,v,w	Velocity components in cylindrical polar (z,r,ϕ) directions
$\tilde{u}_1$	Upstream velocity component normal to a shock

$\tilde{u}_2$	Downstream velocity component normal to a shock
U	τ-dependent vector of conservation-law variables
$\bar{U}$	$\bar{\tau}$-dependent vector of conservation-law variables
$\tilde{U}$	t-dependent vector of conservation-law variables
X,Y,τ	Reference mesh transformed independent variables
$\bar{X},\bar{Y},\bar{\tau}$	Clustered reference mesh transformed independent variables
z,r,ϕ	Cylindrical polar coordinates
α	Angle of attack
γ	Ratio of specific heats
δ_L	Dimensionless bow shock standoff distance at the windward symmetry plane
δ_{SH}	Dimensionless bow shock standoff distance at the cone shoulder
δ_u	Dimensionless bow shock standoff distance at the leeward symmetry plane
$\Delta X,\Delta Y$	Computational reference mesh spacing
$\Delta\bar{X},\Delta\bar{Y}$	Computational clustered reference mesh spacing
$\Delta\theta,\Delta\phi$	Physical plane mesh spacing
$\Delta\Phi$	Shoulder region integration marching step size
$\Delta\nu$	Incremental turning angle
$\Delta\xi$	Shoulder region computational mesh spacing
$\Delta\tau$	Time step for reference mesh integration
$\Delta\bar{\tau}$	Time step for clustered reference mesh integration
ϵ	Fraction of computational mesh spacing
ζ,ξ,Φ	Bow shock aligned, cylindrical polar transformed independent variables
θ_c	Cone half-angle

θ_s	Bow shock shape
θ_{vs}	Vortical singularity position
κ	Parameter in r_{s_ϕ} equation
μ	Magnitude of the gradient of the crossflow shock equation
ρ	Density
σ	Projection of the slope of the characteristics
ϕ_L	Lower meridional boundary
$\phi_{\tilde{s}}$	Crossflow shock shape
$\phi_{\tilde{s}\tilde{\tau}}$	Crossflow shock speed in the ϕ-direction
ϕ_u	Upper meridional boundary
Φ	Meridional independent variable in reference mesh clustering transformation
ψ	Meridional clustering parameter
ω	Theta clustering parameter

Subscripts:

c	Cone surface
cf	Crossflow component
i	Index for discontinuity alignment transformation
J	MacCormack algorithm index for transformed θ-direction differencing in reference mesh
K	MacCormack algorithm index for transformed ϕ-direction differencing in reference mesh
L	Lower meridional boundary
max	Maximum
o	Circular theta outer boundary
o	Meridional plane at center of meridional clustering
rel	Relative to a moving discontinuity

s	Bow shock
$\tilde{s}$	Crossflow shock
S	MacCormack algorithm index for floating shock mesh point
SH	Cone shoulder
SL	MacCormack algorithm index for floating shock mesh point lying below floating shock mesh point S and reference mesh point J
u	Upper meridional boundary
vs	Vortical singularity
X	Unequally spaced mesh in X-direction
$\bar{X}$	$\bar{\tau}$-step size in $\bar{\tau}$, $\bar{X}$-plane
Y	Unequally spaced mesh in Y-direction
$\bar{Y}$	$\bar{\tau}$-step size in $\bar{\tau}$, $\bar{Y}$-plane
∞	Free-stream conditions
1	Shock upstream conditions
1	Vortical singularity, conditions on bow shock side
1,2,3,4,5	Discontinuity alignment transformation
2	Shock downstream conditions
2	Vortical singularity, conditions on cone surface side
*	Windward crossflow sonic line meridional location

Superscripts:

m	Newton-Raphson iteration index
n	Current level in MacCormack algorithm
$\overline{n+1}$	Predictor level in MacCormack algorithm
n+1	Corrector level in MacCormack algorithm
(1)	Surface flow variables following corrector step of MacCormack algorithm

$\vec{\ }$	Vector
$\hat{\ }$	Unit vector

CHAPTER I. INTRODUCTION

Aircraft and missile fuselage geometry can often be approximated by circular or elliptical cones and thus designers have sought methods for computing the inviscid supersonic flow about these shapes. In addition, studies based on simple conical geometry provide a clearer insight into fundamental physical processes for both the experimental and computational investigator.

Busemann (1) pioneered the concept of conical flow defined as a self-similar flow in which fluid properties remain constant along rays emanating from the conical origin. This reduces from three to two the number of independent spatial dimensions in the governing nonlinear partial differential equations. Taylor and Maccoll (2) considered the case of a circular cone at zero angle of attack. The flowfield, being axisymmetric, is determined by only one independent variable thus resulting in a system of ordinary differential equations.

Inclined cones were first treated by Stone (3) as perturbations about the Taylor-Maccoll solutions. Using this method, which is applicable only for small angles of attack, Kopal (4) compiled tables of numerical results. Ferri (5), however, recognized that Stone's method was conceptually wrong near the surface of the cone in that it yields values for the surface entropy that are periodic in the meridional angle. Instead, since the cone surface is a streamline of the flow, the entropy must be invariant. Ferri amended Stone's results by showing that there exists a thin layer of rapidly changing entropy near the cone surface which he labeled the vortical layer. His analysis of the crossflow velocity (the projection of

the velocity vector (Figure 1a) onto the surface of a unit sphere centered at the cone apex (Figure 1b)) revealed that for inviscid conical flow all streamlines must converge to a conical stagnation point in the leeward symmetry plane; the so-called vortical singularity. Since each streamline converging on the vortical singularity has passed through different portions of the bow shock, the entropy, density, and spherical radial velocity component u are multivalued at the singularity.

Based on this theoretical background and early numerical studies a considerable volume of research on nonaxisymmetric conical flows has evolved. Numerous surveys of this work have been presented. Of these, Reference 6 offers the most detailed discussion of many of the methods that have been developed and Reference 7 contains a representative bibliography of the work prior to 1972.

Until recently, however, all techniques have been limited. Even for the simplest conical body, the circular cone, the methods are restricted to cases in which the angle of attack α does not greatly exceed the cone half-angle θ_c or are restricted to solving only the windward portion of the flowfield.

Inverse methods (8, 9), the method of integral relations (10), variations of the method of lines (7, 11 - 14), the method of characteristics (13, 15), as well as the BVLR finite-difference (16, 17) and nonconservative finite-difference formulations (18, 19), encounter difficulties at large angles of attack ($\alpha/\theta_c > 1$). The numerical problems are attributable to the appearance of new flow features on the leeward side of the cone.

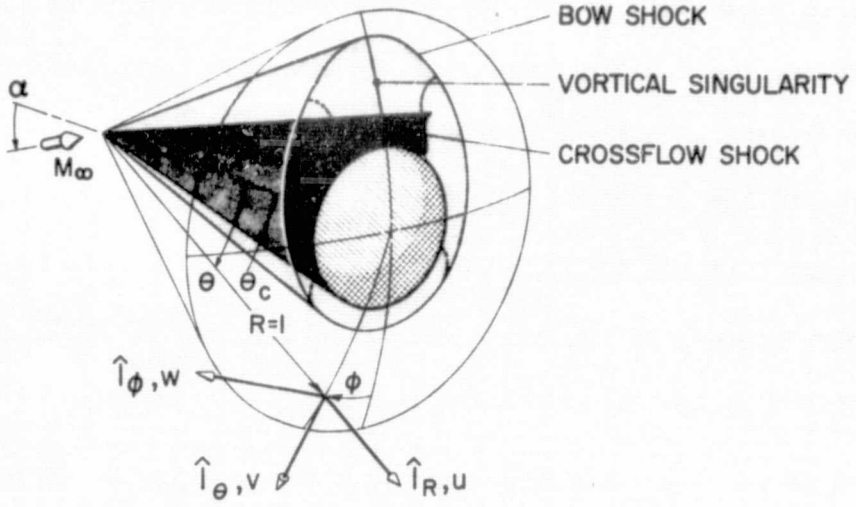

(a) SPHERICAL POLAR COORDINATE SYSTEM AND VELOCITIES

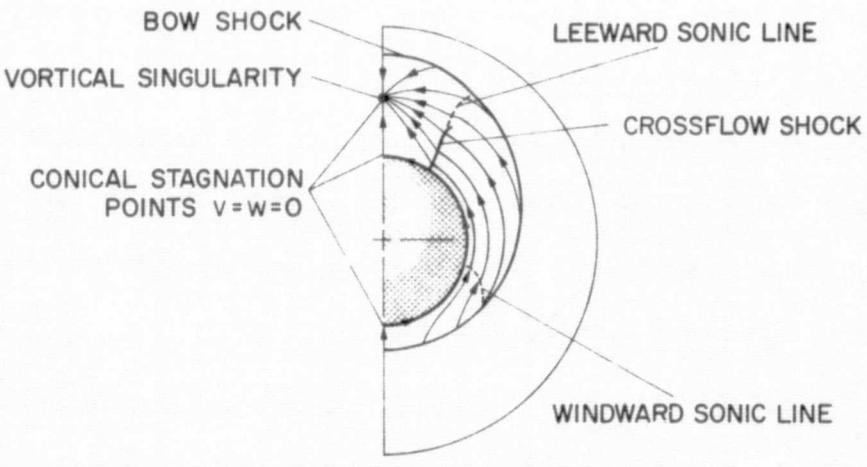

(b) CONICAL STREAMLINES (UNIT SPHERE PROJECTION)

Figure 1. Supersonic flow about a circular cone at large angle of attack, $\alpha/\theta_c > 1$

At moderate angles of attack the crossflow velocity is everywhere subsonic. At large incidence the crossflow accelerates from the windward symmetry plane to supersonic velocities in the shoulder region of the cone. In order to satisfy the leeward symmetry plane boundary conditions, an embedded conical crossflow shock (not present at smaller angles of attack) forms to decelerate the crossflow (Figure 1a, b).

With increasing angle of attack the bow shock gains strength in the windward symmetry plane while becoming weaker on the leeward side, thus the jump in entropy at the vortical singularity intensifies.

The nature of the vortical singularity for cones at large angles of attack has been investigated in several theoretical (5, 20 - 22) and some recent numerical (23, 24) studies. Experimental evidence (25 - 28) indicates that an analogous feature may even be present in viscous flows. The theoretical predictions for the behavior of the vortical singularity are based upon linear theory or localized solutions and thus cannot account for the effects of the crossflow shock. However, the conjecture that the vortical singularity will, at large angles of attack, lift off the cone surface in the leeward symmetry plane (as shown in Figure 1) has been supported by the numerical results (23, 24).

Explicit finite-difference techniques (23, 29 - 31) utilizing the conservation-law form of the governing equations provided the first evidence for the inviscid, nonlinear flow pattern in the leeward region of highly inclined cones. The success of this approach is ascribed to the use of the conservation-law dependent variables. The internal crossflow shock is then automatically captured to within a few mesh intervals.

Improved accuracy is obtained by treating the peripheral bow shock as a sharp discontinuity forming the outer boundary of the computational domain, but the captured vortical singularity remains difficult to resolve. Further, the ability to capture the internal shock is bounded by an upper limit on the range of parameters α/θ_c and the free-stream Mach number M_∞ beyond which the growing strength of the crossflow shock leads to numerical instability. This range has recently been extended by altering the circular shape of the cone on the leeward side (32) or through stress terms added to the governing equations (32, 33). The resulting solutions, however, no longer represent the inviscid cone flowfield.

An investigation preliminary to this study indicated that modifications to the shock-capturing approach, such as the patching of the shock jump conditions at the crossflow shock-cone surface intersection or the selective use of dissipation, affords only limited improvements in resolution and stability.

In contrast to the finite-difference approach, a modification of the method of lines (24, 34) has been used to solve the leeward flow region provided the windward and leeward crossflow sonic lines extend to the bow shock (Figure 2a). The method iterates on the internal shock location but utilizes a bow shock shape extrapolated from the shoulder region. The solutions obtained have been the most extensive to date, particularly in regard to the vortical singularity. The accuracy of the procedure is difficult to assess since there is considerable disagreement with the shock-captured finite-difference results. In addition, it is expected that at large angles of attack the possible nonmonotonic shape of the bow shock

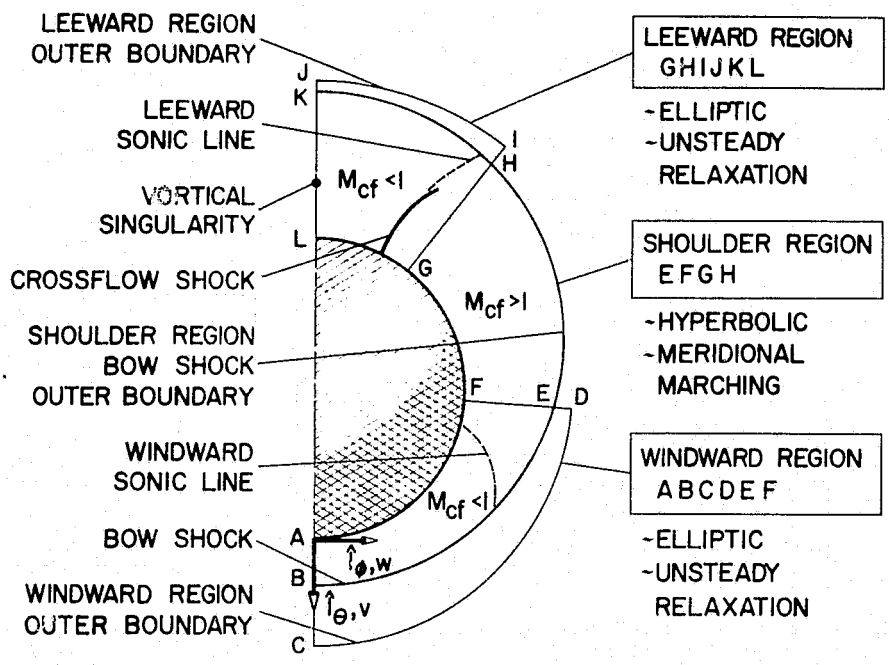

(a) ZONE OF SUPERSONIC CROSSFLOW EXTENDS TO THE BCW SHOCK. HALF-PLANE PARTITIONED INTO THREE SUBPROBLEMS

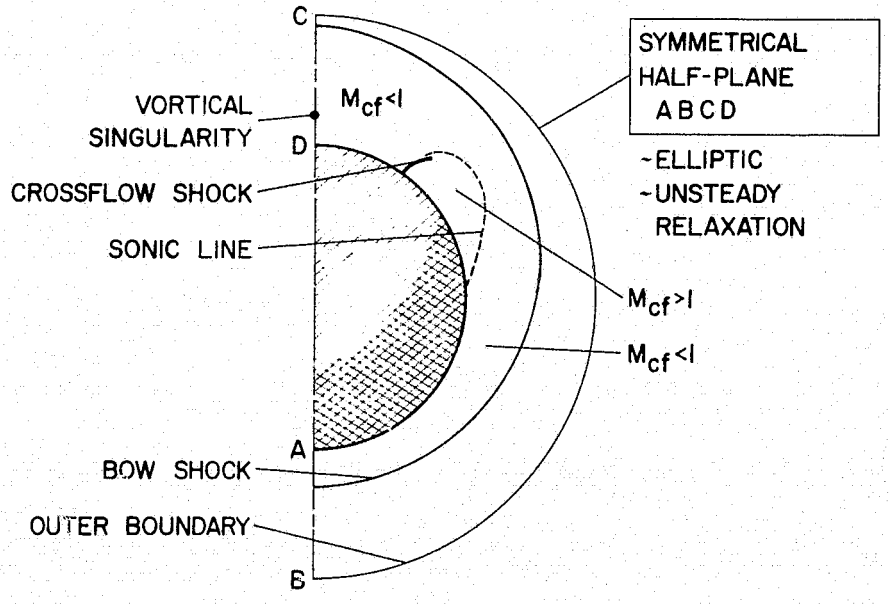

(b) ENCLOSED ZONE OF SUPERSONIC CROSSFLOW. HALF-PLANE PARTITIONING NOT POSSIBLE

Figure 2. Numerical approach determined by the extent of the zone of supersonic crossflow, $M_{cf} = [(v^2 + w^2)/a^2]^{\frac{1}{2}}$

(35) (the maximum shock standoff distance occurring away from the leeward symmetry plane) and its vanishingly weak strength, will dictate a more accurate shock boundary treatment.

An alternative finite-difference method which does not rely on the shock-capturing ability inherent in the conservation-law formulation has been developed in a recent series of reports (36 - 42). Moretti refers to the technique as floating shock fitting to distinguish it from other sharp shock schemes which treat shocks as boundaries of computational domains. In the floating-fitting procedure shocks propagate in the computational domain as discontinuity surfaces. The finite-difference mesh for the computation of the smooth flow regions is fixed and not forced to follow the shocks. Topological problems associated with fitting shocks as boundaries are thereby avoided. However, the differencing scheme must be modified to prevent forming differences across discontinuities and thus involves unequally spaced mesh intervals.

Questions have been raised about the stability and programming complexity of the floating-fitting method for multidimensional flows (43 - 46) and all of the details of the algorithm have not yet been established. Successful applications of the technique, however, have demonstrated the feasibility of the floating-fitting approach. In particular, the method has been tested on the cone at zero incidence problem (37) and gave excellent results.

This present study describes a numerical method which applies the concept of floating shock fitting to the cone at large incidence problem. The bow shock, the embedded crossflow shock, and the vortical singularity

are treated as sharp discontinuities which float simultaneously through the computational mesh. Use is made of the conservation-law form of the governing equations in the flowfield interior to aid in the detection and monitoring of the crossflow shock. The fitting of the crossflow shock avoids the stability problems encountered with the shock-capturing approach. Further, in contrast to the numerical method of References 24 and 34, shock layers with limited zones of supersonic crossflow adjacent to the cone surface (Figure 2b) can be computed. The present method is formulated to be applicable over the complete range of parameters M_∞, α, and θ_c for which the flow remains conical (bow shock wave attached).

Along with the floating-fitting method, a technique in which the bow shock forms a boundary of the computational mesh has been developed. Aside from serving as a check on the floating-fitting approach, this "shock-as-a-boundary" code provides a convenient means of supplying initial conditions for the floating algorithm.

Several boundary condition schemes have been tested in conjunction with the floating-fitting method. Comparisons of these floating-fitting solutions with shock-as-a-boundary results are presented together with numerical results obtained in References 13, 31, and 34 and with experimental measurements (47).

CHAPTER II. GOVERNING EQUATIONS—CHOICE OF VARIABLES

The selection of appropriate dependent and independent variables can simplify the application of a numerical technique and result in improved accuracy. For example, enhanced shock-capturing properties are obtained through the choice of the conservation-law form of the dependent variables in a coordinate system that closely parallels the shock. The implementation of boundary condition schemes, however, may often best be achieved through the use of the primitive dependent variables in a boundary oriented coordinate frame.

Several forms of the governing equations, each chosen with regard to its application and the flow region being computed, are used in the cone at angle of attack problem.

The equations governing the flow of an inviscid, nonconducting, compressible fluid in spherical polar coordinates (Figure 1a) may be arranged into weak conservation-law form as

$$\tilde{U}_t + \tilde{E}_R + \tilde{F}_\theta + \tilde{G}_\phi + \tilde{H} = 0 \tag{1}$$

where $\tilde{U}$, $\tilde{E}$, $\tilde{F}$, $\tilde{G}$, and $\tilde{H}$ are the five-component vectors,

$$\tilde{U} = \begin{Bmatrix} \rho \\ \rho u \\ \rho v \\ \rho w \\ e \end{Bmatrix}, \qquad \tilde{E} = \begin{Bmatrix} \rho u \\ p + \rho u^2 \\ \rho uv \\ \rho uw \\ (e+p)u \end{Bmatrix}, \qquad \tilde{F} = \frac{1}{R} \begin{Bmatrix} \rho v \\ \rho uv \\ p + \rho v^2 \\ \rho vw \\ (e+p)v \end{Bmatrix},$$

$$\tilde{G} = \frac{1}{R \sin\theta} \begin{Bmatrix} \rho w \\ \rho wu \\ \rho wv \\ p + \rho w^2 \\ (e+p)w \end{Bmatrix}, \qquad \tilde{H} = \frac{1}{R} \begin{Bmatrix} \rho(2u + v\cot\theta) \\ \rho(2u^2 - w^2 - v^2 + uv\cot\theta) \\ \rho[3uv + (v^2 - w^2)\cot\theta] \\ \rho w(3w + 2v\cot\theta) \\ (e+p)(2u + v\cot\theta) \end{Bmatrix}. \tag{2}$$

For an ideal gas the system is completed using the equation of state to relate the total energy per unit volume e to the pressure p, density ρ, and velocity components u, v, and w by

$$e = p/(\gamma - 1) + \rho(u^2 + v^2 + w^2)/2 \tag{3}$$

where γ is the ratio of specific heats. The pressure and density are referenced to free-stream static conditions. The velocity components are thus normalized by $a_\infty/\sqrt{\gamma}$ where a_∞ is the free-stream speed of sound.

If the flow is assumed to be steady ($\tilde{U}_t = 0$), the integrated form of the energy equation replaces the last row of Equation (1) with the algebraic relation

$$p = \rho\{[1 + (\gamma - 1)M_\infty^2/2] - [(\gamma - 1)(u^2 + v^2 + w^2)]/2\gamma\} \tag{4}$$

If the flowfield is further assumed to be conical ($\tilde{E}_R = 0$), the governing equations in the self-similar crossflow plane ($R = 1$) become

$$\tilde{F}_\theta + \tilde{G}_\phi + \tilde{H} = 0 \tag{5}$$

Equation (5) is elliptic for cones at small or moderate angles of attack. With increasing incidence a small zone of supersonic crossflow forms adjacent to the surface on the side of the cone (Figure 2b). At still larger angles of attack, the region of supersonic crossflow extends to the bow shock. This enables partitioning of the crossflow plane into windward and leeward elliptic regions separated by the hyperbolic shoulder region (Figure 2a).

In the application of the floating-fitting method, Equation (5) is rendered hyperbolic by the addition of the unsteady derivative term. Alternatively, in the algorithm which fits the bow shock as a boundary,

the spherical radially-asymptotic approach (addition of the conical derivative term) is followed. The unsteady approach is preferred since the hyperbolic nature is preserved over the entire range of parameters M_∞, α, and θ_c for which the bow shock remains attached. Thus, unlike the radially-asymptotic method, the unsteady approach allows computation of radially subsonic flows ($u < a$, where a = local speed of sound) which can occur at large angles of attack (23).

An a priori assumption (based upon previously obtained solutions) can often be made regarding the size of the region of supersonic crossflow. When partitioning of the crossflow plane is possible (Figure 2a), maximum efficiency is achieved by solving each region separately. In addition, for a given number of computational plane grid points resolution is improved since the mesh point density in each region increases. More importantly, the leeward region is freed from the small step size imposed by the stability condition (presented in Chapter III) in the windward symmetry plane. Another benefit of partitioning is that a substantial part of the shoulder region can be computed in one less dimension by a ϕ-direction marching code which integrates the crossflow plane equations. The shoulder region algorithm (described in Appendix A) starts from the windward region outflow boundary (with $w > a$) and sweeps around the cone until the meridional Mach number approaches unity.

Reference Mesh

The floating-fitting procedure utilizes a fixed reference mesh defined by ϕ = constant meridional boundaries and a circular outer boundary $\theta = \theta_o$. An independent variable transformation

$$\left.\begin{aligned} X &= \frac{\theta - \theta_c}{\theta_o - \theta_c} \\ Y &= \phi \\ \tau &= t \end{aligned}\right\} \tag{6}$$

normalizes the cone-to-outer boundary distance. The reference mesh for the leeward region calculation is illustrated in Figure 3.

The transformation Equation (6) distinguishes the floating-fitting technique from shock-as-a-boundary methods (cf. Equation (A4)) and reduces the complexity of the flowfield interior transformed governing equations. This simplification is important in the leeward region where the shock-as-a-boundary approach requires normalizations in two directions.

A further transformation $(\bar{X}, \bar{Y}, \bar{\tau})$, which permits clustering points near the cone surface and about a chosen meridional location (48), may be used to concentrate points near the crossflow shock. Clustering is also useful in keeping the number of reference mesh points that lie outside of the shock layer (where no calculations take place) to a minimum. This is especially helpful when solving the symmetrical half-plane (Figure 2b) problem since the bow shock is often far from being circular. The clustered reference mesh independent variables are defined by

$$\left.\begin{aligned} \bar{X} = \bar{X}(X) &= \frac{1}{\omega} \sinh^{-1}[X \sinh \omega] \\ \bar{Y} = \bar{Y}(Y) &= \frac{\Phi_{max}}{\psi} \left\{ B + \sinh^{-1}\left[\left(\frac{\Phi}{\Phi_o} - 1 \right) \sinh B \right] \right\} \\ \bar{\tau} = \bar{\tau}(\tau) &= \tau \end{aligned}\right\} \tag{7}$$

where

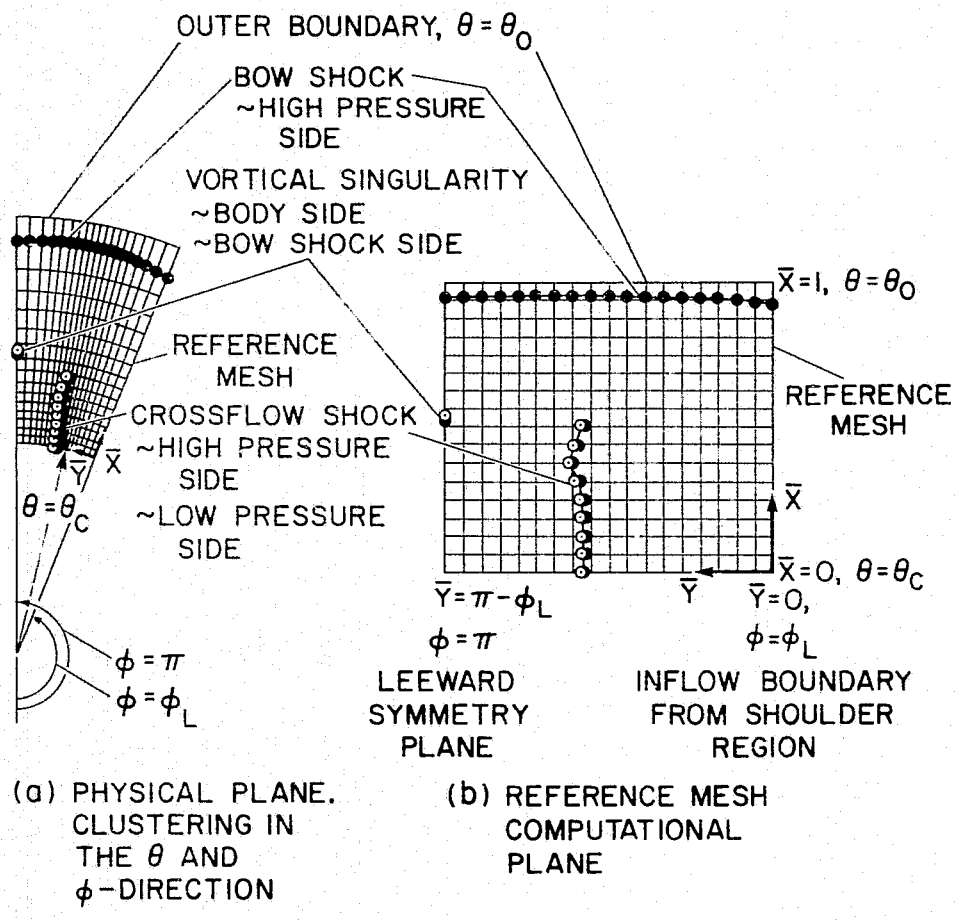

Figure 3. Floating discontinuities in the leeward region reference mesh

$$\left.\begin{aligned} \Phi &= Y - \phi_L \\ \Phi_{max} &= \phi_u - \phi_L \\ \Phi_o &= \phi_o - \phi_L \\ B &= \frac{1}{2} \ln \left[\frac{1 + (e^{\psi} - 1) \dfrac{\Phi_o}{\Phi_{max}}}{1 + (e^{-\psi} - 1) \dfrac{\Phi_o}{\Phi_{max}}} \right] \end{aligned}\right\} \tag{8}$$

with

ϕ_L = lower meridional boundary

ϕ_u = upper meridional boundary

ψ = meridional clustering parameter, clustering about ϕ_o

ω = theta clustering parameter, clustering about θ_c

Application of the clustering transformation (Equation (7)) to the conical Euler equations in spherical polar coordinates (Equation (1) with $\tilde{E}_R = 0$) and rearrangement into weak conservation-law form yields the system

$$\bar{U}_{\bar{\tau}} + \bar{F}_{\bar{X}} + \bar{G}_{\bar{Y}} + \bar{H} = 0 \tag{9}$$

where

$$\left.\begin{aligned} \bar{U} &= \tilde{U} \\ \bar{F} &= \frac{1}{\theta_o - \theta_c} \bar{X}_X \tilde{F} \\ \bar{G} &= \bar{Y}_Y \tilde{G} \\ \bar{H} &= \tilde{H} - \frac{1}{\theta_o - \theta_c} (\bar{X}_X)_{\bar{X}} \tilde{F} - (\bar{Y}_Y)_{\bar{Y}} \tilde{G} \end{aligned}\right\} \tag{10}$$

The first derivatives of the clustered mesh independent variables appearing in Equation (10) are

$$\left.\begin{aligned} \bar{X}_X &= \frac{\sinh \omega}{\omega \cosh(\omega \bar{X})} \\ \bar{Y}_Y &= \frac{\left(\frac{\Phi_u}{\Phi_o}\right) \sinh B}{\psi \sqrt{\left[\left(\frac{\Phi}{\Phi_o} - 1\right) \sinh B\right]^2 + 1}} \end{aligned}\right\} \tag{11}$$

and the second derivatives required to form the $\bar{H}$ vector are

$$\left.\begin{aligned} (\bar{X}_X)_{\bar{X}} &= \frac{-\sinh \omega \sinh(\omega \bar{X})}{\cosh^2(\omega \bar{X})} \\ (\bar{Y}_Y)_{\bar{Y}} &= \frac{-\left(\frac{\Phi}{\Phi_o} - 1\right) \sinh^2 B}{\Phi_o \left\{1 + \left[\left(\frac{\Phi}{\Phi_o} - 1\right) \sinh B\right]^2\right\}} \end{aligned}\right\} \tag{12}$$

The number of reference mesh points in the $\bar{X}$ and $\bar{Y}$-directions, the outer boundary location θ_o, and the clustering parameters ω, ψ, and ϕ_o, are specified in a separate code as part of the initialization procedure for the floating-fitting code (initial conditions are discussed in Chapter IV). This mesh generation code offers an interactive option in which the mesh variables may be iteratively adjusted. The resulting distribution of grid points in the physical domain is displayed on a cathode ray tube (C.R.T.) following each mesh specification (IBM 360/67 time-sharing system linked to an IBM 2250 C.R.T.).

Once an initial reference mesh is selected, it remains fixed in the unsteady relaxation procedure. Thus the geometric derivatives, which

appear as coefficients of the $\tilde{F}$ and $\tilde{G}$ vectors in Equation (10), need only be evaluated initially for each mesh point.

Floating Discontinuity Points

The floating-fitting technique also employs discontinuity oriented coordinate systems, each normalizing the distance between a fixed boundary and a moving discontinuity (Figure 3). The necessary transformations are presented in Table 1.

The governing equations are integrated on one side of each discontinuity. At embedded shock discontinuities, the integration is performed on the low pressure side. At the vortical singularity, the integration is performed on the low entropy side (either side may be used). The low pressure side integration, however, is not required at the peripheral bow shock since the flowfield is the known free stream. The flow values on the remaining side of each discontinuity are obtained, once the new discontinuity geometry has been determined, from the discontinuity jump conditions.

The form of the Euler equations suitable for all discontinuity alignment transformations on the unit sphere is

$$d_{\bar{\tau}} + [\bar{B}_1]\, d_{\bar{X}} + [\bar{B}_2]\, d_{\bar{Y}} + A_3 = 0 \tag{13}$$

where

$$d = \begin{Bmatrix} p \\ u \\ v \\ w \\ e \end{Bmatrix}, \qquad A_3 = \begin{Bmatrix} a^2\rho\,(2u + v\,\cot\theta) \\ -(v^2 + w^2) \\ uv - w^2\,\cot\theta \\ w(u + v\,\cot\theta) \\ (e + p)\,(2u + v\,\cot\theta) \end{Bmatrix} \tag{14}$$

Table 1. Discontinuity alignment transformations

Coordinate system	θ-direction	ϕ-direction
Reference mesh	$X = \frac{\theta - \theta_c}{\theta_o - \theta_c}$	$Y = \phi$
Bow shock, high-pressure side[a]	$X_1 = \frac{\theta - \theta_c}{\theta_s - \theta_c}$	$Y_1 = Y$
Crossflow shock, low-pressure side[b,c]	$X_2 = X$	$Y_2 = \frac{\phi - \phi_L}{\phi_{\tilde{s}} - \phi_L}$
Crossflow shock, high-pressure side[b,c]	$X_3 = X$	$Y_3 = \frac{\phi - \phi_u}{\phi_u - \phi_{\tilde{s}}}$
Vortical singularity, bow shock side[d]	$X_4 = \frac{\theta - \theta_o}{\theta_o - \theta_{vs}}$	$Y_4 = Y$
Vortical singularity, body side[d]	$X_5 = \frac{\theta - \theta_c}{\theta_{vs} - \theta_c}$	$Y_5 = Y$

[a] $\theta_s = \theta_s(\phi,t)$ ~ bow shock shape

[b] $\phi_{\tilde{s}} = \phi_{\tilde{s}}(\theta,t)$ ~ crossflow shock shape

[c] ϕ_L, ϕ_u ~ lower and upper meridional boundaries

[d] $\theta_{vs} = \theta_{vs}(t)$ ~ vortical singularity position

with

$$\left.\begin{aligned}[\bar{B}_1] &= \{X_\theta[A_1] + X_\phi[A_2] + X_t[I]\}\bar{X}_X \\ [\bar{B}_2] &= \{Y_\theta[A_1] + Y_\phi[A_2] + Y_t[I]\}\bar{Y}_Y\end{aligned}\right\} \tag{15}$$

where $[I]$ is the identity matrix and

$$[A_1] = \begin{bmatrix} v & 0 & a^2\rho & 0 & 0 \\ 0 & v & 0 & 0 & 0 \\ 1/\rho & 0 & v & 0 & 0 \\ 0 & 0 & 0 & v & 0 \\ v & 0 & e+p & 0 & v \end{bmatrix},$$

$$[A_2] = \frac{1}{\sin\theta}\begin{bmatrix} w & 0 & 0 & a^2\rho & 0 \\ 0 & w & 0 & 0 & 0 \\ 0 & 0 & w & 0 & 0 \\ 1/\rho & 0 & 0 & w & 0 \\ w & 0 & 0 & e+p & w \end{bmatrix} \tag{16}$$

The derivatives of the reference mesh independent variables are evaluated for each alignment transformation $i = 1, 2, 3, 4, 5$ (Table 1) by application of the chain rule where

$$\left.\begin{aligned} X_\phi &= X_\theta\,\theta_{X_i}\,X_{i_\phi} \\ X_t &= X_\theta\,\theta_{X_i}\,X_{i_t} \\ Y_\theta &= Y_\phi\,\phi_{Y_i}\,Y_{i_\theta} \\ Y_t &= Y_\phi\,\phi_{Y_i}\,Y_{i_t}\end{aligned}\right\} \tag{17}$$

with $X_\theta = 1/(\theta_o - \theta_c)$ and $Y_\phi = 1$.

To integrate Equation (13), the reference mesh derivatives (listed in Table 2) are evaluated at each discontinuity. The coefficients of: θ_{s_ϕ}, θ_{s_t}, θ_{vs_t}, $\phi\tilde{s}_\theta$, and $\phi\tilde{s}_t$ in Table 2, then reduce to -1.

The nonconservative form of the governing equations (Equation (13)) does not require evaluation of the second derivatives of the transformed

Table 2. Reference mesh independent variable derivatives

Coordinate System	X-direction			Y-direction		
	X_θ	X_ϕ	X_t	Y_θ	Y_ϕ	Y_t
Spherical polar	1	0	0	0	1	0
Reference mesh	$\frac{1}{\theta_o - \theta_c}$	0	0	0	1	0
Bow shock, high-pressure side	$\frac{1}{\theta_o - \theta_c}$	$\frac{-X}{\theta_s - \theta_c}\theta_{s_\phi}$	$\frac{-X}{\theta_s - \theta_c}\theta_{s_t}$	0	1	0
Crossflow shock, low-pressure side	$\frac{1}{\theta_o - \theta_c}$	0	0	$\frac{-(Y - \phi_L)}{\phi_{\tilde{s}} - \phi_L}\phi_{\tilde{s}_\theta}$	1	$\frac{-(Y - \phi_L)}{\phi_{\tilde{s}} - \phi_L}\phi_{\tilde{s}_t}$
Crossflow shock, high-pressure side	$\frac{1}{\theta_o - \theta_c}$	0	0	$\frac{-(Y - \phi_u)}{\phi_{\tilde{s}} - \phi_u}\phi_{\tilde{s}_\theta}$	1	$\frac{-(Y - \phi_u)}{\phi_{\tilde{s}} - \phi_u}\phi_{\tilde{s}_t}$
Vortical singularity, bow shock side	$\frac{1}{\theta_o - \theta_c}$	0	$\frac{-(X - 1)}{\theta_{vs} - \theta_o}\theta_{vs_t}$	0	1	0
Vortical singularity, body side	$\frac{1}{\theta_o - \theta_c}$	0	$\frac{-X}{\theta_{vs} - \theta_c}\theta_{vs_t}$	0	1	0

independent variables. These terms, which contribute to the source vector of the conservation-law system (see, for example, Equation (10)), are absent in the nonconservative system.

The choice of circular geometry for the reference mesh is responsible for the simple scaling which relates derivatives along discontinuities and derivatives in the discontinuity normalized direction to the reference mesh system. The finite-difference representation of Equation (13) for a discontinuity integration does not require grid points located at ΔX_i and ΔY_i (Table 1) intervals. Each discontinuity mesh consists solely of points lying on the discontinuity and being tracked along one of the reference mesh directions (Figure 3).

CHAPTER III. FINITE-DIFFERENCE METHOD

MacCormack's explicit, second-order, noncentered, predictor-corrector algorithm (49) (presented in Appendix B) is used to advance the flowfield in the time-asymptotic relaxation process. The algorithm's low storage requirements and ease of programming make it readily adaptable to a floating-fitting approach. With floating-fitting, the standard MacCormack scheme is modified for mesh points which lie on the boundaries and floating discontinuities; and for points neighboring (in time or space) the floating discontinuities. In the reference mesh interior the forward-predictor, backward-corrector sequence is followed provided the computational molecule is not crossed by a discontinuity.

Special Discretization Formulas

The floating-fitting technique introduces unequally spaced mesh intervals. Special differencing approximations (36), formulated to maintain stability and accuracy, replace the two-point uniformly spaced approximations used at each level in the MacCormack algorithm. The derivation of these differencing approximations is based upon weighting the contributions of neighboring mesh points (on the same side of a discontinuity) in such a way that the truncation error varies smoothly as the discontinuity cuts through the mesh.

Reference mesh points

At a given time level, the presence of a discontinuity adjacent to a reference mesh point will prevent forming the standard spatial difference. In addition, the temporal derivative must be discarded if, in advancing

to the next level, the reference mesh point passes from one side of the discontinuity to the other.

Temporal derivatives The floating-fitting algorithm keeps track of the location of moving discontinuities relative to the fixed reference mesh. Movement of discontinuities over reference mesh points generally occurs only during the early transient phase. Consider the integration of

$$U_T + F_X + G_Y + H = 0 \tag{18}$$

where

$$\left.\begin{aligned} U &= \tilde{U} \\ F &= \frac{1}{\theta_o - \theta_c}\tilde{F} \\ G &= \tilde{G} \\ H &= \tilde{H} \end{aligned}\right\} \tag{19}$$

using MacCormack's scheme. Referring to Figure 4, if the shock point S is located between reference mesh points J and J-1 at time level n and crosses point J (moving in the X-direction) while advancing to time level $\overline{n+1}$, then $U_J^{\overline{n+1}}$ is computed by the linear interpolation

$$U_J^{\overline{n+1}} = \frac{1}{1+\epsilon_X}\left(U_S^{\overline{n+1}} + \epsilon_X U_{J-1}^{\overline{n+1}}\right) \tag{20}$$

Spatial derivatives The replacement of reference mesh spatial derivatives is illustrated in Figure 4. The approximation (Salas, M., private communication, NASA-Langley Research Center, 1976) shown for F_{X_J} was found to yield results equivalent to those obtained using a formula that involved an additional point in the reference mesh (37). The removal of even one point offers coding simplifications.

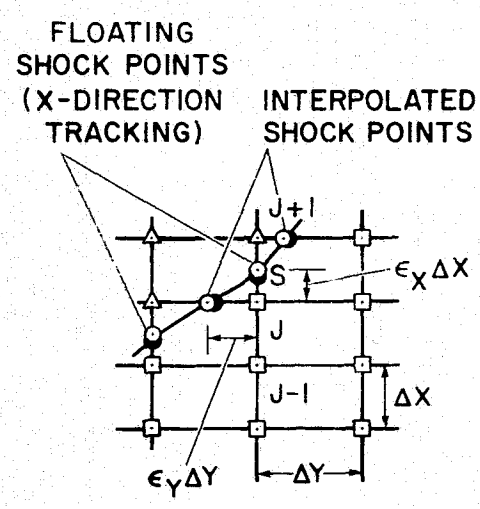

REFERENCE MESH
COMPUTATIONAL
PLANE

DIFFERENCE APPROXIMATION FOR $\frac{\partial F}{\partial X}$

AT SHOCK POINT S:

$$F_{X_S} = \frac{1}{\Delta X}\left[\left(\frac{3}{1+\epsilon_X}\right)F_S - 2F_J + \left(\frac{2\epsilon_X - 1}{1+\epsilon_X}\right)F_{J-1}\right]$$

AT REFERENCE MESH POINT J:
IN THE FORWARD PREDICTOR STEP,
REPLACE

$$F_{X_J} = \frac{F_{J+1} - F_J}{\Delta X}$$

BY

$$F_{X_J} = \frac{1}{\Delta X}\left[\frac{2(2-\epsilon_X)}{1+\epsilon_X} F_S + (2\epsilon_X - 3)F_J + \frac{(1-\epsilon_X)(2\epsilon_X - 1)}{1+\epsilon_X} F_{J-1}\right]$$

Figure 4. Spatial differencing approximations for floating-fitting

If the shock in Figure 4 also cuts the mesh interval J to J-1, so that F_{J-1} is not available for the computation of F_{X_J}, then F_{X_J} is approximated by

$$F_{X_J} = \frac{F_S - F_{SL}}{X_S - X_{SL}} \tag{21}$$

where S and SL represent shock points lying above and below the reference mesh point J.

If point J is on an X-boundary, so that no points are below it, then F_{X_J} is computed using

$$F_{X_J} = \frac{F_S - F_J}{\epsilon_X \Delta X} \quad \text{for} \quad \epsilon_X \geq \frac{1}{2} \tag{22}$$

for $\epsilon_X < 1/2$, F_{X_J} is obtained by extrapolation of F_X in the Y-direction.

Similar discretization formulas apply to the required Y-derivatives at point J. However, since shock points are tracked only along Y = constant lines (for the example shown in Figure 4) interpolation is required to obtain G_S values where the shock cuts a ΔY mesh interval. Linear interpolation has been found to be sufficient.

If the independent variable clustering transformation $(\bar{X}, \bar{Y}, \bar{\tau})$ (Equation (7)) has been applied to the reference mesh, then interpolations are performed in the unequally spaced physical plane. The conservation-law vector in the computational plane $\bar{G}_S$ (Equation (10)) is obtained by multiplying the interpolated $\tilde{G}_S$ vector by the clustered mesh $\bar{Y}_Y$ geometric derivative. The geometric derivative is computed analytically

(Equation (11)) using the interpolated location of the intersection of the shock with the physical plane $\Delta\phi$ mesh interval. Interpolated distances are transformed to the computational plane and the appropriate special differencing formula applied.

Discontinuity mesh points Derivatives along the shock in Figure 4 are computed using the usual MacCormack scheme. Derivatives in the shock normalized direction, obtainable in terms of X-derivatives, are computed using the F_{X_S} Equation (42) shown in Figure 4.

The same derivative approximations are used at the crossflow shock and at the bow shock except that the roles of X and Y are interchanged. Bow shock points are tracked in the X-direction while crossflow shock points move in the Y-direction.

X-derivatives at the vortical singularity are similar to those at bow shock points since the vortical singularity is also tracked in the X-direction. For the Y-derivative at the vortical singularity (w_Y being the only nonzero Y-derivative), interpolated reference mesh values must be used.

Stability Analysis

Although a two-dimensional analysis is appropriate, one-dimensional amplification matrix theory yields a larger, yet stable, estimate for the step size. The influence of the discontinuity alignment transformations is reflected by the derivatives of X and Y (Equation (17)) appearing in the C-F-L condition (Courant-Friedrichs-Lewy)

$$\Delta\bar{\tau} = \min(\Delta\bar{\tau}_{\bar{X}}, \Delta\bar{\tau}_{\bar{Y}}) \tag{23}$$

where

$$\left.\begin{aligned} \Delta\bar{\tau}_{\bar{X}} &= \frac{(CN)\Delta\bar{X}}{|\sigma_{max}([\bar{B}_1])|} \\ \Delta\bar{\tau}_{\bar{Y}} &= \frac{(CN)\Delta\bar{Y}}{|\sigma_{max}([\bar{B}_2])|} \end{aligned}\right\} \tag{24}$$

with

$$\left.\begin{aligned} |\sigma_{max}([\bar{B}_1])| &= \max|\sigma([\bar{B}_1])|_i \\ |\sigma_{max}([\bar{B}_2])| &= \max|\sigma([\bar{B}_2])|_i \end{aligned}\right\} \tag{25}$$

where $i = 1, 2, 3, 4, 5$ (Table 1), and with the projections of the characteristic slopes (eigenvalues) determined by

$$\left.\begin{aligned} |\sigma([\bar{B}_1])| &= \bar{X}_X\left[\left|X_\theta v + \frac{X_\phi w}{\sin\theta} + X_t\right| + a\sqrt{X_\theta^2 + \left(\frac{X_\phi}{\sin\theta}\right)^2}\right] \\ |\sigma([\bar{B}_2])| &= \bar{Y}_Y\left[\left|Y_\theta v + \frac{Y_\phi w}{\sin\theta} + Y_t\right| + a\sqrt{Y_\theta^2 + \left(\frac{Y_\phi}{\sin\theta}\right)^2}\right] \end{aligned}\right\} \tag{26}$$

The Courant parameter, CN in Equation (24), by linear analysis must be ≤ 1. For most floating-fitting applications CN is set to 0.9.

Accuracy and Convergence

In the unsteady analysis, the total enthalpy (which should approach that of the free stream in the converged solution) serves as a convenient measure of accuracy. For example, for a typical leeward region calculation with a reference mesh containing 17 points in the X-direction and 19 points in Y-direction the total enthalpy at interior mesh points differs from the free-stream total enthalpy by much less than 0.1%. Larger errors generally are found on the cone surface or near the vortical singularity

(results are presented in Chapter VI). However, the total enthalpy error at these boundary points stays well below 1%.

The total enthalpy is also used to verify the achievement of a steady state by testing for negligible change between current values and those computed 10 iterations before. Due to the extensive use of interactive graphics and a time-sharing system, meaningful convergence times are difficult to obtain. Roughly, a 17×19 mesh requires less than 15 minutes on an IBM 360/67 to achieve convergence.

CHAPTER IV. INITIAL CONDITIONS

Free-stream conditions or very approximate initial guesses are often sufficient to initiate a shock-capturing relaxation procedure. Somewhat more care is required in specifying the initial flowfield when a peripheral shock is computed by a shock fitting approach. If all discontinuities are to be fitted, the determination of initial conditions can become very involved. In the case of a cone at large angle of attack the problem is further complicated by the difficulty of obtaining a physically relevant flowfield that can evolve into the desired conical flow. For many cases of interest, the idea of starting with a sphere-cone solution is ruled out by the failure of existing sphere-cone codes at large angles of attack. At smaller angles of attack, where solutions can be obtained, the presence of strong entropy gradients from the blunt nose may require special treatment.

The initialization procedure for the floating-fitting algorithm is illustrated schematically in Figure 5. Essentially, the strategy is to start from a flowfield obtained by choosing shock shape and surface distribution parameters or by using previously computed solutions with nearly the same values of M_∞, θ_c, and α. This starting flow is then further refined by iterating with the code which fits the bow shock as a boundary and captures embedded discontinuities. Only a few iterations are required to establish a flowfield that is suitable for the floating-fitting technique to adequately detect the forming embedded discontinuities. Instabilities that may arise with the capturing code, if strong crossflow shocks are present, are avoided by beginning the floating-fitting technique in the early stages of shock formation.

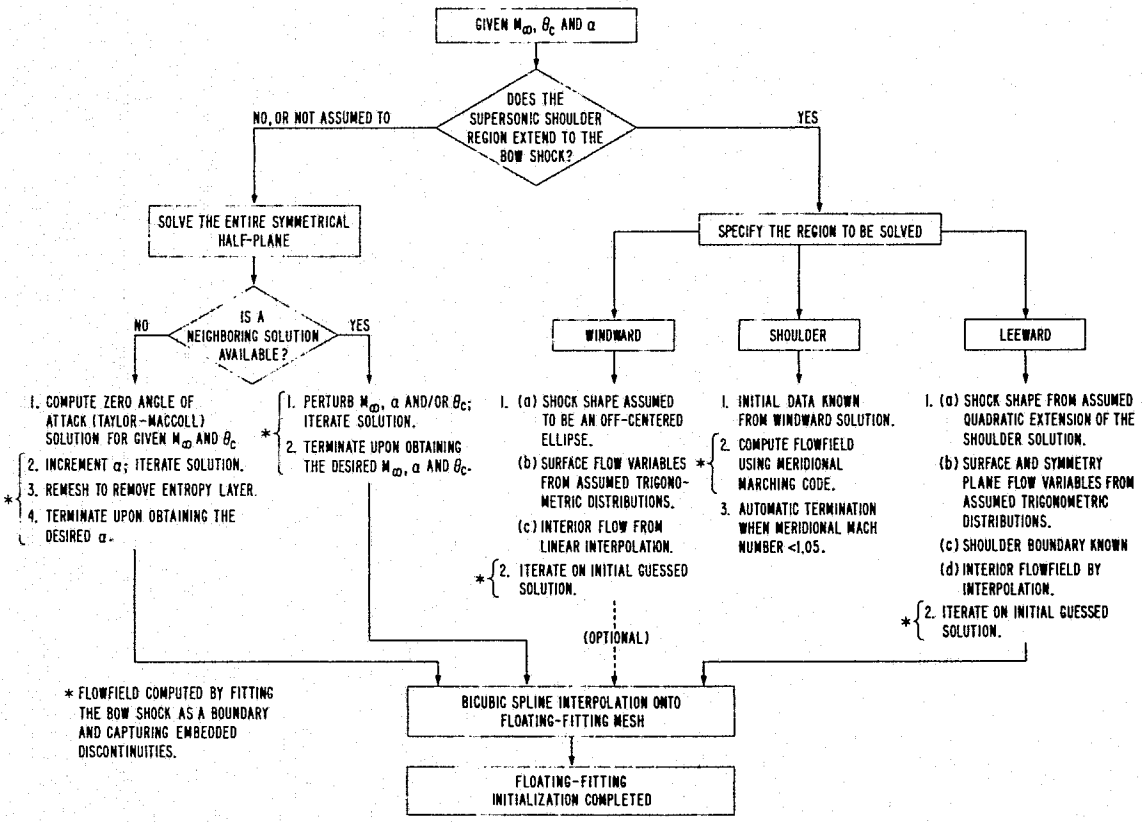

Figure 5. Determination of initial conditions for the floating-fitting scheme

Bow Shock Shape

As shown in Figure 5, initialization of the windward and leeward regions requires an estimate for the bow shock shape. Some empirical correlation formulas have been proposed for the windward region bow shock shape (see, for example, Reference 9), however, a more convenient estimate is provided by a scheme suggested in Reference 18. The shape of the bow shock, of which only the windward portion is used, is assumed to be an off-centered ellipse when projected onto the cylindrical (r, ϕ) plane perpendicular to the cone centerline (the z-axis). In the cylindrical polar coordinate system, as adopted in Appendix A, ϕ is measured from the windward symmetry plane. Denoting the bow shock cylindrical radius as r_s and the cone surface as r_c, the initial bow shock shape (at $z = 1$) is

$$r_s(\phi) = \frac{-C \cos\phi + B\sqrt{\frac{(B^2 - C^2)}{A^2} \sin^2\phi + \cos^2\phi}}{\left(\frac{B}{A}\right)^2 \sin^2\phi + \cos^2\phi} \tag{27}$$

where the parameter C is the distance in the symmetry plane that the center of the ellipse is offset from the center of the coordinate system $(r = 0)$. The parameters A and B are, respectively, the semiminor and semimajor axes of the ellipse. In terms of the dimensionless shock standoff distance in the windward symmetry plane δ_L, at the cone shoulder δ_{SH}, and in the leeward symmetry plane δ_u, the ellipse parameters are

$$\left.\begin{aligned} B &= r_c\left(1 + \frac{\delta_L + \delta_u}{2}\right) \\ C &= \frac{r_c}{2}(\delta_u - \delta_L) \\ A &= \frac{r_c\,(\delta_{SH} + 1)}{\sqrt{1 - \left(\frac{C}{B}\right)^2}} \end{aligned}\right\} \tag{28}$$

where the standoff distances are normalized by the cone radius.

The number of parameters that must be guessed is reduced from three to two by the introduction of the empirical correlation (18), known to be valid over a wide range of Mach numbers and angles of attack (though untested at angles of attack exceeding the cone half-angle),

$$\tan^{-1}[(1 + \delta_u)\tan\theta_c] = 2\theta_s\Big|_{\alpha=0} - \tan^{-1}[(1 + \delta_{SH})\tan\theta_c] \tag{29}$$

where θ_s is the bow shock angle corresponding to the zero angle of attack Taylor-Maccoll (2) solution.

The leeward region initial bow shock may be determined without guessing shape parameters. A quadratic extension of the shoulder region bow shock is completely determined by the conditions of matching the known shock slope and standoff distance at the lower meridional boundary and by satisfying the zero slope condition at the leeward symmetry plane. For some cases, this quadratic shock may intersect the free-stream Mach cone. If a test reveals that bow shock mesh points lie within the free-stream Mach cone, an incremental shock standoff distance is added. The bow shock is moved outward a trial amount in the leeward symmetry plane. The incremental function is specified as a cubic in ϕ satisfying zero slope con-

straints at both leeward region meridional boundaries. The function decreases from the trial value in the leeward symmetry plane to zero at the lower meridional (shoulder) boundary.

Distribution of Flow Variables

As indicated, the difficult task of specifying an initial flowfield for the floating-fitting code that may include embedded discontinuities is alleviated by first iterating on a rough initial flowfield approximation utilizing the capturing capabilities of the shock-as-a-boundary code.

The procedure used to obtain the rough initial flowfield approximation may be illustrated by considering the windward region problem. Here the nondimensionalizations are those used in the shock-as-a-boundary code and described in Appendix A.

At the bow shock, the analytically prescribed bow shock shape together with the known free-stream conditions and an assumed zero shock speed are sufficient to determine all downstream shock values. The appropriate shock jump conditions are given in the Shock Boundary section of Appendix A.

At the cone surface, a guess of the windward stagnation point pressure $p_c(0)$ is the only parameter that is required. Based on previous windward solutions, the pressure decrease around the cone may be approximated by

$$p_c(\phi) = \frac{1}{2}\left[(p_c(0) + p_\infty) + (p_c(0) - p_\infty)\cos\phi\right] \tag{30}$$

where p_∞ is the free-stream pressure.

The surface entropy is constant and assumed to equal that behind the bow shock in the windward symmetry plane, denoted as S_c. Thus, surface

density is given by

$$\rho_c(\phi) = \left(\frac{p_c(\phi)}{S_c}\right)^{\frac{1}{\gamma}} \tag{31}$$

The velocity modulus is obtained from the condition of constant total enthalpy as

$$q_c(\phi) = \sqrt{1 - \frac{p_c(\phi)}{\rho_c(\phi)}} \tag{32}$$

The windward region meridional outflow boundary ϕ_u is assumed to be positioned downstream of the crossflow sonic line. On the cone surface the w-velocity component must satisfy the supersonic outflow condition as well as the symmetry plane condition that $w = 0$ at $\phi = 0$.

A linear increase in w is assumed according to

$$w_c(\phi) = \sqrt{\frac{(\gamma - 1)\, p(\phi_*)}{2\, \rho(\phi_*)}}\, \frac{\phi}{\phi_*} \tag{33}$$

where the crossflow sonic line intersects the body at $\phi = \phi_*$ which is specified as $\phi_* = \frac{5}{6}\phi_u$.

Combining constant total enthalpy (Equation (32)) with the tangency condition yields the remaining cylindrical polar velocity components (Appendix A)

$$u_c(\phi) = \sqrt{\frac{q_c(\phi)^2 - w_c(\phi)^2}{1 + r_{c_z}^2}} \tag{34}$$

and

$$v_c(\phi) = u_c(\phi)\, r_{c_z} \tag{35}$$

Linear interpolation between the surface and bow shock furnishes the interior flowfield pressure, density, w- and v-velocity components with the u-velocity component calculated to satisfy total enthalpy.

In the windward symmetry plane the linear density distribution is replaced in order to maintain the streamline entropy S_c. The symmetry plane linear pressure distribution is accepted with the density determined as in Equation (31).

A similar procedure is followed to obtain a rough initial flowfield approximation for the leeward region problem (Figure 5). The main difference with the windward region technique is that the inflow meridional plane flow values are known. The leeward interior flowfield is computed as an average of a linear interpolation between assumed shock and surface distributions and a linear interpolation in the meridional direction between assumed symmetry plane values and known inflow conditions.

CHAPTER V. BOUNDARY CONDITIONS

In the shock-as-a-boundary approach, which captures embedded discontinuities, the physical plane bow shock layer boundaries are mapped onto rectangular computational plane boundaries. The flow tangency condition is imposed on the impermeable cone surface and symmetry planes. As a part of the relaxation process, use is made of the asymptotic condition that the surface and symmetry plane entropy can vary only through discontinuous jumps at the vortical singularity and at the crossflow shock-cone surface intersection. Of the permeable boundaries, the shock-as-a-boundary bow shock is governing by the Rankine-Hugoniot shock jump relations while the meridional boundaries encountered in the windward, shoulder, and leeward region subproblems are either known inflow boundaries or boundaries where the flow is assumed to be outflowing supersonically.

The floating-fitting approach is distinguished from the capturing approach by imposing jump conditions across discontinuities that do not form reference mesh computational plane boundaries (Figure 3). The floating vortical singularity is an impermeable point in the crossflow plane projection while the floating bow and crossflow shocks are permeable surfaces with, respectively, known and unknown upstream flow conditions.

One-Sided Differencing

The implementation of boundary condition schemes at reference mesh points on the cone surface and the symmetry plane involves the evaluation of derivatives normal to these surfaces. Similarly, at floating mesh points on each side of a discontinuity, derivatives in the discontinuity

normalized direction are required. The normalized direction, as defined in Table 1, is not necessarily the normal direction since the alignment transformations are nonorthogonal.

At the reference mesh boundaries the normal direction derivatives are evaluated using equally spaced, three-point, one-sided approximations in both the predictor and corrector steps of MacCormack's algorithm provided a discontinuity is not encountered. The use of three-point difference approximations is in keeping with the second-order of the algorithm. Suitable one-sided approximations at reference mesh boundary points in the vicinity of discontinuities, and for floating mesh points, have been given in the Special Discretization Formulas section of Chapter III.

Cone Surface

The shock-as-a-boundary code employs Abbett's (50) Euler predictor/simple wave corrector procedure at the cone surface. The application of the scheme for the shoulder region problem is presented in Appendix A. Reference 31 outlines a version of Abbett's scheme similar to that adapted in the shock-as-a-boundary, radially-asymptotic, windward region code where the surface entropy is assigned the value behind the bow shock in the symmetry plane.

A modification to Abbett's scheme has been devised to account for the jump in entropy at the crossflow shock occurring in the leeward and symmetrical half-plane problems. The technique falls short of the accuracy obtainable with a properly formulated shock fitting procedure but is a vast improvement over the isentropic Abbett scheme. The modified scheme

also eliminates the entropy oscillations neighboring the crossflow shock that occur using the nonisentropic Abbett scheme presented in Reference 51.

In the radially-asymptotic, shock-as-a-boundary approach, the modification to Abbett's scheme is applied following the corrector step of the nonisentropic Abbett procedure (51). Denote these corrected surface flow values as $\tilde{p}$, $\tilde{\rho}$, $\tilde{u}$, $\tilde{v}$, and $\tilde{w}$. Here the velocity components are in the cylindrical polar coordinate (z, r, ϕ) directions and the nondimensionalizations are as presented in Appendix A. Let the modified surface flow values be denoted by p, ρ, u, v, and w and let the subscripts 1 and 2 designate, respectively, the crossflow shock upstream and downstream conditions.

The pressure from the Abbett scheme expansion or compression is not altered by the modification procedure, that is, at the z^{n+1} step,

$$p(\phi) = \tilde{p}(\phi) \tag{36}$$

This surface pressure distribution is scanned and the crossflow shock is assumed to lie within the mesh interval containing the maximum compressive pressure gradient.

Least-squares fit polynomials (2nd-degree) are passed through the pressure data lying on the crossflow upstream and downstream sides of this mesh interval providing approximations for the pressures at the crossflow shock of the form

$$p_1(\phi) = a\phi^2 + b\phi + c \tag{37}$$

$$p_2(\phi) = d\phi^2 + e\phi + f \tag{38}$$

The crossflow upstream density distribution follows, once the upstream side has been identified, by imposing on the cone surface the value of

entropy obtained at the bow shock in the windward symmetry plane, denoted as S_1. Thus,

$$\rho(\phi) = \left(\frac{p(\phi)}{S_1}\right)^{\frac{1}{\gamma}} \tag{39}$$

The velocity components, which satisfy surface tangency after the turn in Abbett's scheme, are proportioned to satisfy constant total enthalpy by the relations

$$\left.\begin{aligned} u &= \tilde{u}\frac{q_1}{\tilde{q}} \\ v &= \tilde{v}\frac{q_1}{\tilde{q}} \\ w &= \tilde{w}\frac{q_1}{\tilde{q}} \end{aligned}\right\} \tag{40}$$

where the velocity moduli are

$$\left.\begin{aligned} \tilde{q} &= \sqrt{1 - \frac{p_1}{\rho_1}} \\ q &= \sqrt{1 - \frac{p}{\rho}} \end{aligned}\right\} \tag{41}$$

The upstream surface crossflow Mach number

$$M_{cf} = \frac{w}{\sqrt{\frac{\gamma - 1}{2}\frac{p}{\rho}}} \tag{42}$$

is computed at each mesh point and a least-squares fit quadratic approximation is obtained for the upstream Mach number at the crossflow shock as

$$M_{cf_1}(\phi) = g\phi^2 + h\phi + i \tag{43}$$

The location of the crossflow shock within the mesh interval containing the maximum compressive pressure gradient is computed by solving for that $\phi = \phi_{\tilde{s}}$ which satisfies the normal shock Rankine-Hugoniot jump condition

$$p_2(\phi) = p_1(\phi)\left[\frac{2\gamma M^2_{cf_1}(\phi) - (\gamma - 1)}{\gamma + 1}\right] \tag{44}$$

Equation (44) is solved iteratively using the Newton-Raphson technique

$$\phi^m_{\tilde{s}} = \phi^{m-1}_{\tilde{s}} - \frac{L\left(\phi^{m-1}_{\tilde{s}}\right)}{L'\left(\phi^{m-1}_{\tilde{s}}\right)} \tag{45}$$

where m is the iteration index and

$$L(\phi) = (\gamma + 1)(d\phi^2 + e\phi + f) + (a\phi^2 + b\phi + c)[(\gamma - 1) - 2\gamma(g\phi^2 + h\phi + i)^2] \tag{46}$$

The mesh interval mid-point serves as the initial guess for $\phi_{\tilde{s}}$.

With $\phi_{\tilde{s}}$ determined, the crossflow shock entropy jump is given by

$$S_2 = S_1 \frac{\left[\frac{2\gamma M^2_{cf_1} - (\gamma - 1)}{\gamma + 1}\right]}{\left[\frac{(\gamma + 1)M^2_{cf_1}}{(\gamma - 1)M^2_{cf_1} + 2}\right]^\gamma} \tag{47}$$

The crossflow downstream modified surface density and velocity distributions are computed, in the same manner as on the upstream side, but with the value of entropy S_2 being imposed.

The floating-fitting code uses Kentzer's surface boundary conditions (52) in conjunction with the MacCormack algorithm in a two-step procedure analogous to that proposed in Reference 19. Also, included as an option

in the floating-fitting code, is a simple boundary condition scheme termed a one-sided differencing approach.

In the one-sided differencing scheme the conservation-law form of the gas dynamic equations (Equation (9)), with the tangency condition $v = 0$, is integrated on the cone surface. The resulting values for total energy e and the velocity components u and w are accepted. Recall that in the floating-fitting, time-asymptotic code the velocity components u, v, and w are with respect to a spherical polar (R, θ, ϕ) coordinate system and the nondimensionalizations are as described in Chapter II. Surface pressure is computed by iteratively solving (using Newton-Raphson) the nonlinear equation relating p to the total energy e

$$e = bp + cp^{\frac{1}{\gamma}} \tag{48}$$

where

$$\left.\begin{aligned} b &= \frac{1}{\gamma - 1} \\ c &= \frac{u^2 + w^2}{2S^{\frac{1}{\gamma}}} \end{aligned}\right\} \tag{49}$$

The value of entropy S appearing in the c coefficient is set to the appropriate crossflow shock upstream or downstream value. This surface entropy at the new time level is determined in a preliminary calculation which advances the floating bow shock only in the windward symmetry plane (not required if solving just the leeward region) and the floating crossflow shock only at the cone surface. With p and S known, a new density

is obtained (see Equation (39)) and used to recompute all but the last row of the $\tilde{U}$ vector (Equation (2)).

Kentzer's surface boundary scheme is an approximation of exact characteristics theory which eliminates the interpolations and iterations required in following characteristic directions in a fixed mesh.

The approach combines the differentiated surface tangency condition ($v_{\bar{\tau}} = 0$) with the compatibility relation along the down-running characteristic in the $\bar{X}$, τ-plane resulting in a differential equation for the surface pressure

$$p_{\bar{\tau}} = (ap_{\bar{X}} - \gamma p v_{\bar{X}}) \frac{\bar{X}_X}{\theta_o - \theta_c} - (wp_{\bar{Y}} + \gamma p w_{\bar{Y}}) \frac{\bar{Y}_Y}{\sin \theta_c} - a\rho (2au + w^2 \cot \theta_c) \qquad (50)$$

With $v = 0$, the remaining velocity components u and w are computed using respectively the R and ϕ-momentum equations, the second and fourth rows of Equation (13)

$$u_{\bar{\tau}} = - w \frac{\bar{Y}_Y}{\sin \theta_c} u_{\bar{Y}} + w^2 \qquad (51)$$

and

$$w_{\bar{\tau}} = - \left(\frac{1}{\rho} p_{\bar{Y}} + w w_{\bar{Y}} \right) \frac{\bar{Y}_Y}{\sin \theta_c} - uw \qquad (52)$$

Derivatives along the cone surface ($\bar{Y}$-direction) are approximated by the MacCormack forward-backward sequence or, if neighboring a discontinuity, by special discretization formulas (Chapter III). The only exception being the $w_{\bar{Y}}$ derivative in Equation (52) which is always approximated by backward differences (19).

As in the one-sided scheme, the surface entropy at the new time level is obtained in a preparatory step by advancing the floating shocks. The updated density is computed with the specified entropy and the pressure from Equation (39). Equation (13), for the total energy, need not be integrated, instead, e is obtained from Equation (3).

Kentzer's scheme is modified for surface mesh points in the symmetry planes (which are conical stagnation ($v = w = 0$) points). The symmetry conditions

$$\left.\begin{aligned} w &= 0 \\ p_{\bar{Y}} = u_{\bar{Y}} &= v_{\bar{Y}} = e_{\bar{Y}} = 0 \end{aligned}\right\} \tag{53}$$

are applied and thus Equation (52) is discarded. Note that u cannot be obtained directly by integration since, upon substitution of $w = 0$, Equation (51) reduces to

$$u_{\bar{\tau}} = 0 \tag{54}$$

One method to allow for relaxation of the u-velocity component is to introduce the $e_{\bar{\tau}}$ equation, the last row of Equation (13). Further, at the conical stagnation points $e_{\bar{\tau}}$ is related to $p_{\bar{\tau}}$ by

$$e_{\bar{\tau}} = \frac{(e+p)}{\gamma p} p_{\bar{\tau}} \quad (\text{at} \quad \phi = 0, \pi) \tag{55}$$

With e known, u follows from Equation (3).

Inflow and Outflow Meridional Boundaries

The three subproblems making up the partitioned half-plane (Figure 2a) are joined by meridional inflow and outflow boundaries.

In the windward region the outflow boundary must be selected a priori such that it lies beyond the limiting characteristic in the crossflow plane. Extrapolation then provides flow values along the boundary. Where possible, second-order, equally-spaced extrapolation is used. However, since the floating bow shock may cut across the reference mesh it is necessary to also allow for unequally spaced data obtained by interpolating bow shock values.

The shoulder region ϕ-marching code (Appendix A) obtains initial data from the converged windward solution. The w-velocity must be supersonic all along the initial data line. The ϕ-direction sweep around the cone is terminated when the w-velocity drops to sonic speed. In practice, a cut-off of $w = 1.05a$ is used since the ϕ-step size approaches zero as w approaches a.

The leeward region inflow boundary flow variables are held fixed at values prescribed by the shoulder region code. The initial meridional plane is selected such that the crossflow Mach number always exceeds unity.

Symmetry Planes

Imposing the symmetry conditions, Equations (53), on the first four rows of Equation (13) yields the three equations to be integrated at the windward and leeward symmetry planes. The symmetry conditions are also applied in the calculation of the vortical singularity and in the calculation of the body and bow shock points at the symmetry planes.

As with the $w_{\bar{y}}$ derivative in Equation (52), the differencing of $v_{\bar{x}}$ in the $v_{\bar{t}}$ equation should be made in accordance with the sign of the

v-velocity (19). Additionally, special discretization is required at points neighboring the vortical singularity in the leeward symmetry plane.

The updated entropy is specified above and below the vortical singularity and e computed as in the body boundary calculation.

Symmetry conditions may also be applied to the conservation-law form of the governing equations (Equation (9)). If the conservation-law form is integrated in the leeward symmetry plane, no special treatment is given to the vortical singularity.

Discontinuities

The bow shock in the shock-as-a-boundary code is calculated following Thomas' "pressure approach" (48). Its adaptation to the shoulder region problem is detailed in Appendix A. In the windward, leeward, and symmetrical half-plane problems the use of Thomas' scheme is similar to the application discussed in Reference 31.

The floating-fitting technique utilizes Kentzer's characteristics based approach (52) to propagate the bow shock, the embedded crossflow shock, and the vortical singularity.

Detection and monitoring

Embedded discontinuities are searched for in the flowfield provided by the initial condition procedure (Chapter IV). The floating vortical singularity is initially positioned at a weighted location within the mesh interval having the maximum density gradient in the leeward symmetry plane.

Crossflow shock points are detected by continually scanning the pressure distribution along θ = constant lines. Trial floating shock points are positioned at a weighted location within the mesh interval having the maximum compressive gradient (as computed by the conservation-law form of the governing equations). With extrapolated upstream flow values and a finite-difference approximation for the shock slope, a normal Mach number is computed. If the normal Mach number is greater than one, then tracking of the trail shock point as a shock point begins.

A check for embedded shock points is made after each advancement, with points being added or discarded. The embedded shock forms early and locks into place near the cone surface. However, the end-point of the embedded shock tends to oscillate. In order to eliminate this problem, without the complications of treating the true shock tip (41), an artificial cutoff of the fitted shock is made. Some small overshoots and undershoots, typical of shock-captured solutions, are observed at the truncated shock tip. However, these small errors do not propagate away from the tip region.

In practice, the simplest of several schemes used to terminate the crossflow shock is to specify a priori a θ-boundary beyond which the crossflow shock is captured.

Propagation

Combining a characteristic compatibility relation with the differentiated discontinuity jump conditions yields an equation for the acceleration of the discontinuity. The updated discontinuity speed and position is obtained by integrating its acceleration using a second-order Euler predictor/modified Euler corrector method.

The updated flow values on one side of the discontinuity are obtained by integrating the nonconservative form of the discontinuity aligned governing equations (Equation (13)), with the exception of the bow shock where one side is the known free stream. At the crossflow shock, the governing equations are integrated on the low pressure (crossflow upstream) side. At the vortical singularity, the integration is performed on the low entropy (bow shock) side.

With the updated geometry and flow values known on one side, the updated flow values on the opposite side of the discontinuity are determined by the jump conditions.

The implementation of Kentzer's scheme may be illustrated by considering the propagation of the crossflow shock. Crossflow shock points are tracked in the $\bar{Y}$-direction. Using the notation and definitions shown in Figure 6, $q_{\tilde{S}_{\bar{\tau}}}$ represents the acceleration of the crossflow shock, normal to the shock and pointing towards the high pressure side. The equation for the crossflow shock acceleration (with clustering in the reference mesh) obtained by combining the compatibility relation along the down-running characteristic in the $\bar{Y}_3$, $\bar{\tau}$-plane (Table 1) with the $\bar{\tau}$-differentiated Rankine-Hugoniot jump conditions, is

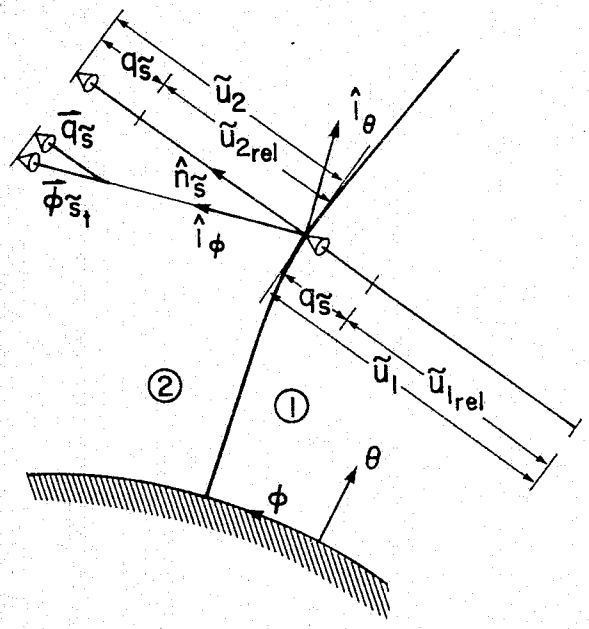

$$\hat{n}_{\tilde{s}} = \tilde{n}_\theta \hat{i}_\theta + \tilde{n}_\phi \hat{i}_\phi$$

$$\text{WHERE } \tilde{n}_\theta = \frac{-\phi_{\tilde{s}_\theta}}{\mu}, \; \tilde{n}_\phi = \frac{1}{\mu \sin\theta}$$

$$\text{WITH } \quad \mu = \sqrt{\phi^2_{\tilde{s}_\theta} + \left(\frac{1}{\sin\theta}\right)^2}$$

$$\vec{q}_{\tilde{s}} = q_{\tilde{s}} \hat{n}_{\tilde{s}} = \left(\frac{\phi_{\tilde{s}_t}}{\mu}\right) \hat{n}_{\tilde{s}}$$

$$\vec{\tilde{u}}_1 = \tilde{u}_1 \hat{n}_{\tilde{s}} = \left(V_1 \tilde{n}_\theta + W_1 \tilde{n}_\phi\right) \hat{n}_{\tilde{s}}$$

$$\tilde{u}_{1_{rel}} = \tilde{u}_1 - q_{\tilde{s}}, \; \tilde{u}_{2_{rel}} = \tilde{u}_2 - q_{\tilde{s}}$$

Figure 6. Crossflow shock geometry and motion

$$q_{\tilde{s}_{\bar{\tau}}} = \tilde{R}_1 (\tilde{R}_2 + \tilde{R}_3 + \sigma\tilde{R}_4 + \tilde{R}_5 + \tilde{R}_6) \tag{56}$$

where

$$\tilde{R}_1 = \frac{\gamma + 1}{2\left\{2\rho_1 \tilde{u}_{1_{rel}} + a\rho\left[1 + \left(\frac{1}{\tilde{M}_{1_{rel}}}\right)^2\right]\right\}}$$

$$\tilde{R}_2 = \frac{\tilde{u}_{1_{\bar{\tau}}}}{\gamma + 1}\left\{4\rho_1 \tilde{u}_{1_{rel}} - a\rho\left[(\gamma - 1) - 2\left(\frac{1}{\tilde{M}_{1_{rel}}}\right)^2\right]\right\}$$

$$+ \frac{p_{1_{\bar{\tau}}}}{\gamma + 1}\left[2\gamma \tilde{M}^2_{1_{rel}} - (\gamma - 1)\right] - \frac{4a_{1_{\bar{\tau}}}}{\gamma + 1}\left(\rho_1 \tilde{u}_{1_{rel}} \tilde{M}_{1_{rel}} + \frac{a\rho}{\tilde{M}_{1_{rel}}}\right)$$

$$\tilde{R}_3 = a\rho\left(v\tilde{n}_{\theta_{\bar{\tau}}} + w\tilde{n}_{\phi_{\bar{\tau}}}\right)$$

$$\tilde{R}_4 = [p_{\bar{Y}} - a\rho(\tilde{n}_\theta v_{\bar{Y}} + \tilde{n}_\phi w_{\bar{Y}})]Y_{\bar{Y}}$$

$$\tilde{R}_5 = \frac{1}{\theta_o - \theta_c}\left\{(v - a\tilde{n}_\theta)p_{\bar{X}} + a\rho[(a - v\tilde{n}_\theta)v_{\bar{X}} - v\tilde{n}_\phi w_{\bar{X}}]\right\}\bar{X}_X$$

$$\tilde{R}_6 = a\rho\{a(2u + v\cot\theta) - [\tilde{n}_\theta(uv - w^2\cot\theta) + \tilde{n}_\phi w(u + v\cot\theta)]\}$$

In Equation (56), the down-running characteristic is defined by

$$\sigma = -\phi\tilde{s}_\theta v + \frac{w}{\sin\theta} - \phi\tilde{s}_t - a\mu \tag{57}$$

the upstream normal relative Mach number is

$$\tilde{M}_{1_{rel}} = \frac{\tilde{u}_{1_{rel}}}{a_1} \tag{58}$$

and the nonsubscripted flow values represent the crossflow shock downstream conditions.

The crossflow shock acceleration (Equation (56)) is used to update the normal component of the shock velocity and the shock position according to

the two-step sequence

Predictor:

$$\overline{q^{n+1}_{\tilde{s}}} = q^{n}_{\tilde{s}} + q^{n}_{\tilde{s}_{\bar{\tau}}} \Delta\bar{\tau} \tag{59}$$

$$\overline{\phi^{n+1}_{\tilde{s}}} = \phi^{n}_{\tilde{s}} + \phi^{n}_{\tilde{s}_{\bar{\tau}}} \Delta\bar{\tau} \tag{60}$$

Corrector:

$$q^{n+1}_{\tilde{s}} = q^{n}_{\tilde{s}} + \frac{1}{2}\left(\overline{q^{n+1}_{\tilde{s}_{\bar{\tau}}}} + q^{n}_{\tilde{s}_{\bar{\tau}}}\right) \Delta\bar{\tau} \tag{61}$$

$$\phi^{n+1}_{\tilde{s}} = \phi^{n}_{\tilde{s}} + \frac{1}{2}\left(\overline{\phi^{n+1}_{\tilde{s}_{\bar{\tau}}}} + \phi^{n}_{\tilde{s}_{\bar{\tau}}}\right) \Delta\bar{\tau} \tag{62}$$

As is shown in Figure 6, the component of the shock velocity in the ϕ-direction is related to the normal component by

$$\phi_{\tilde{s}_{\bar{\tau}}} = \phi_{\tilde{s}_t} = \sqrt{\phi^2_{\tilde{s}_\theta} + \left(\frac{1}{\sin\theta}\right)^2}\, q_{\tilde{s}} \tag{63}$$

With the updated crossflow shock low pressure side flow values, the upstream velocity component normal to the crossflow shock is given by

$$\tilde{u}_1 = v_1 \tilde{n}_\theta + w_1 \tilde{n}_\phi \tag{64}$$

and, relative to a shock moving with velocity $q_{\tilde{s}}$,

$$\tilde{u}_{1_{rel}} = \tilde{u}_1 - q_{\tilde{s}} \tag{65}$$

Application of the Rankine-Hugoniot relations yields

$$p_2 = \left[\frac{2\gamma \tilde{M}^2_{1_{rel}} - (\gamma - 1)}{\gamma + 1}\right] p_1 \tag{66}$$

$$\tilde{u}_{2_{rel}} = \frac{a}{\gamma + 1}\left[\frac{2}{\tilde{M}_{1_{rel}}} + (\gamma - 1)\,\tilde{M}_{1_{rel}}\right] \tag{67}$$

$$\rho_2 = \frac{\tilde{u}_{1_{rel}}}{\tilde{u}_{2_{rel}}} \rho_1 \tag{68}$$

The u-velocity component (velocity in R-direction) is tangential to the crossflow shock and hence remains unchanged

$$u_2 = u_1 \tag{69}$$

The remaining downstream velocity components are

$$v_2 = (\tilde{u}_{2_{rel}} - \tilde{u}_{1_{rel}})\,\tilde{n}_\theta + v_1 \tag{70}$$

$$w_2 = (\tilde{u}_{2_{rel}} - \tilde{u}_{1_{rel}})\,\tilde{n}_\phi + w_1 \tag{71}$$

With the velocity components determined, the total energy is obtained from Equation (3).

The propagation of the bow shock is analogous to, but much simpler than, that described for the embedded crossflow shock.

The motion of the vortical singularity in the leeward symmetry plane is, following Kentzer's approach, governed by

$$q_{vs_{\bar{T}}} = \frac{1}{\rho_1 a_1 + \rho_2 a_2}\left\{[(a_1 + a_2)p_{\bar{X}} + \gamma p(v_{2_{\bar{X}}} - v_{1_{\bar{X}}})] \times \frac{\bar{X}_X}{\theta_o - \theta_c} + 2\gamma p(u_2 - u_1)\right.$$
$$\left. - q_{vs}(a_1 \rho_1 u_1 + a_2 \rho_2 u_2)\right\} \tag{72}$$

where q_{vs} is the speed of the vortical singularity, positive pointing towards the body, and where the subscripts 1 and 2 represent, respectively, the bow shock and body sides of the singularity.

Prior to advancing the vortical singularity, the bow shock in the leeward symmetry plane and the crossflow shock at the cone surface are advanced to make available the updated values of leeward symmetry plane entropy, denoted as S_1 and S_2.

With the updated position and speed of the vortical singularity, together with the bow shock side (side 1) flow values, the body side pressure is given by the continuity of pressure across the singularity

$$p_2 = p_1 \tag{73}$$

and the absence of a normal relative velocity component yields the body side v-velocity

$$v_2 = v_1 = -q_{vs} \tag{74}$$

Equating total enthalpy across the singularity yields an equation for the R-direction velocity component

$$u_2 = \left[\frac{2\gamma}{\gamma - 1}\left(\frac{p_1}{\rho_1} - \frac{p_2}{\rho_2}\right) + u_1^2\right]^{\frac{1}{2}}$$

then Equation (3) is used to compute e_2.

Alternatively, the total enthalpy need not be equated across the singularity provided the $e_{\bar{\tau}}$ or $u_{\bar{\tau}}$ equation is integrated on the body side of the singularity.

Variable area effect

As noted in References 39 and 41, shock acceleration equations can be very sensitive to the manner in which they are discretized. The crossflow shock acceleration Equation (56) is no exception.

Following the suggestions in Reference 39, the $\tilde{R}$ terms in Equation (56) have been grouped according to their differing physical roles. The accurate calculation of $\tilde{R}_5$ requires that the $v_{\bar{X}}$ and $w_{\bar{X}}$ difference approximations include discontinuity mesh points which lie midway between the

mesh points being tracked. The inclusion of this so-called "variable-area" effect thus doubles the number of discontinuity mesh points. The location of these intermediate mesh points is determined by the points being tracked. The evaluation of side 1 temporal derivatives at the intermediate mesh points introduces the further complication of obtaining upstream flow values by interpolation in the reference mesh. However, with these added mesh points the tendency of the crossflow shock to develop kinks is removed.

CHAPTER VI. RESULTS AND DISCUSSION

The partitioning of the crossflow plane into separate windward, shoulder, and leeward region problems (Figure 2a) is demonstrated by solving the case: $M_\infty = 7$, $\theta_c = 20°$, and $\alpha = 30°$. With this choice of parameters, results of the floating-fitting method can be compared with those obtained in Reference 34 using the GTT modified method of lines approach.

Additional windward region results are obtained for the case: $M_\infty = 7.95$, $\theta_c = 10°$, and $\alpha = 16°$ to compare the numerical floating-fitting solution with experimental measurements reported in Reference 47. The comparison is made on the windward side of the cone where viscous effects are small. Experimental data on the leeward side cannot be used to verify the numerical method since discrepancies would be due primarily to the inappropriateness of the inviscid model to describe the viscous dominated region near the cone surface and in the symmetry plane.

The symmetrical half-plane problem (Figure 2b), where partitioning of the crossflow plane is not possible, is demonstrated by computing the case: $M_\infty = 3$, $\theta_c = 7.5°$, and $\alpha = 15°$. In Reference 31, a solution obtained using a finite-difference method based on the shock-capturing approach (for embedded discontinuities) is available for comparison.

The stability and accuracy of the floating-fitting technique was first tested on the windward region problem, thus avoiding the additional complexity of embedded discontinuities. Also, several boundary condition schemes were assessed using windward region calculations.

Figure 7 shows the solution for the floated bow shock shape in the reference mesh compared with the shock-as-a-boundary results and a method of lines solution (34). The corresponding density distribution behind the bow shock is plotted in Figure 8 with the method of lines solution from Reference 13. The floating-fitting, shock-as-a-boundary, and method of lines results are in excellent agreement. Numerous crossings of the reference mesh θ = constant grid lines (Figure 7) are demonstrated to have no adverse effect on the floating-fitting solution.

Body boundary condition methods are compared in Figure 9 for a windward region case where experimental values are also available (47). The numerical methods all tend to produce the same result. The differences between the numerical and experimental pressures are primarily due to experimental errors (12, 52) with viscous effects being negligible (53).

It might be expected that Kentzer's body boundary scheme, based on the theory of characteristics, will yield the most accurate solution. However, the windward region results in Figure 9 do not distinguish one body boundary procedure as being superior. This close agreement of the various techniques is most likely due to the use of coordinates and velocity components (independent and dependent variables) which are in the surface normal and tangential directions.

In Figure 10, the solution from the shoulder region ϕ-marching code is shown together with the windward region results in the form of crossflow plane contour plots. The acceleration around the cone shoulder is demonstrated by the crossflow Mach number levels in Figure 10a. The windward

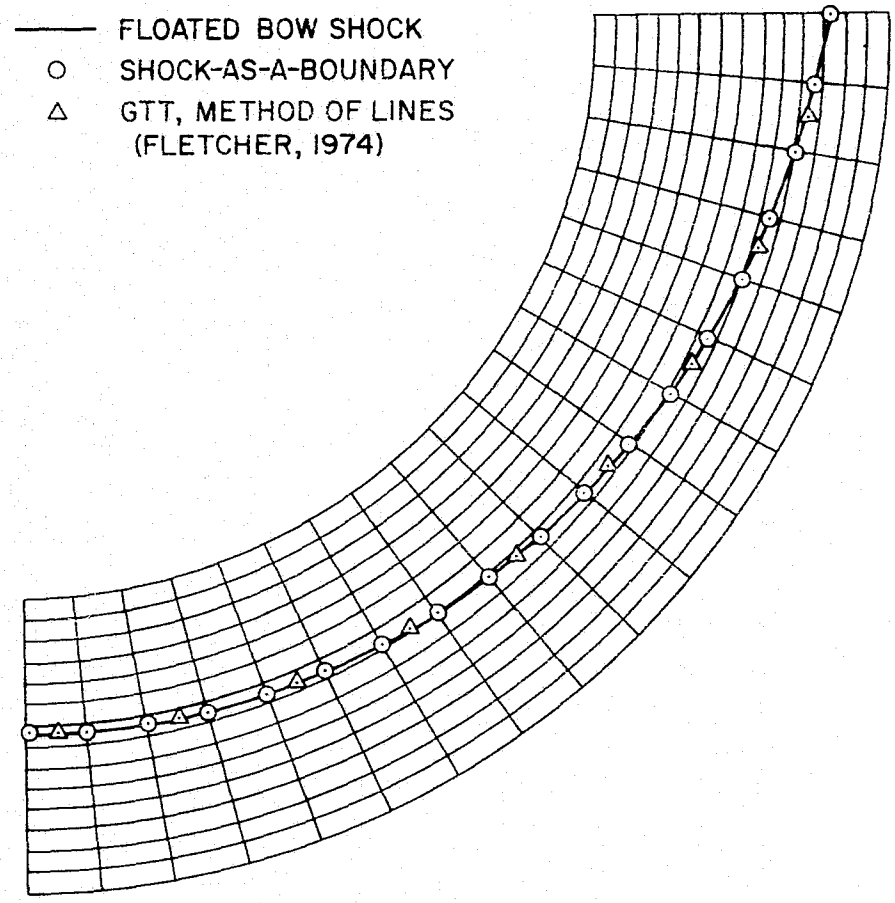

Figure 7. Floated bow shock in the windward region reference mesh. Comparison of bow shock shapes; $M_\infty = 7$, $\theta_c = 20°$, $\alpha = 30°$

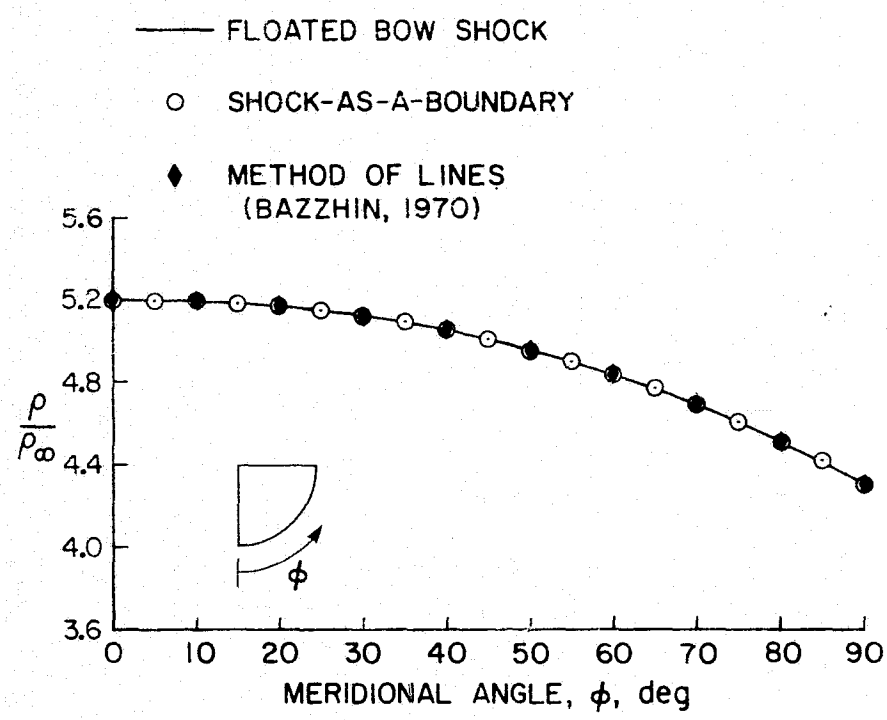

Figure 8. Density distribution behind the bow shock in the windward region; $M_\infty = 7$, $\theta_c = 20°$, $\alpha = 30°$

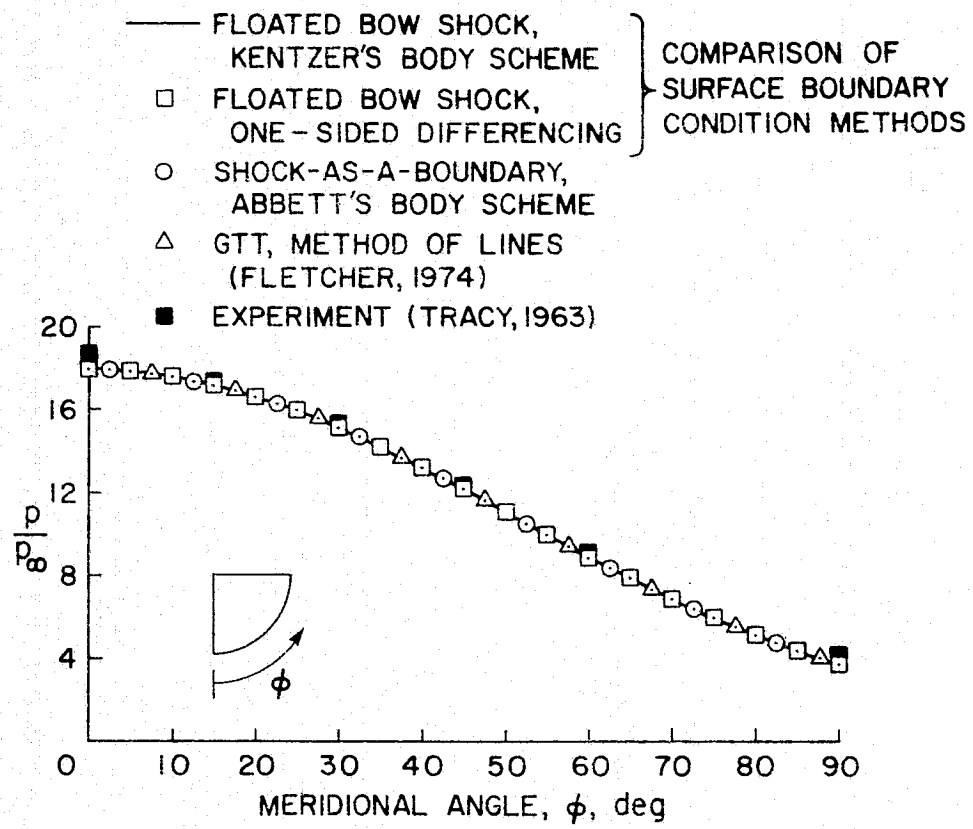

Figure 9. Surface pressure distribution in the windward region; $M_\infty = 7.95$, $\theta_c = 10°$, $\alpha = 16°$

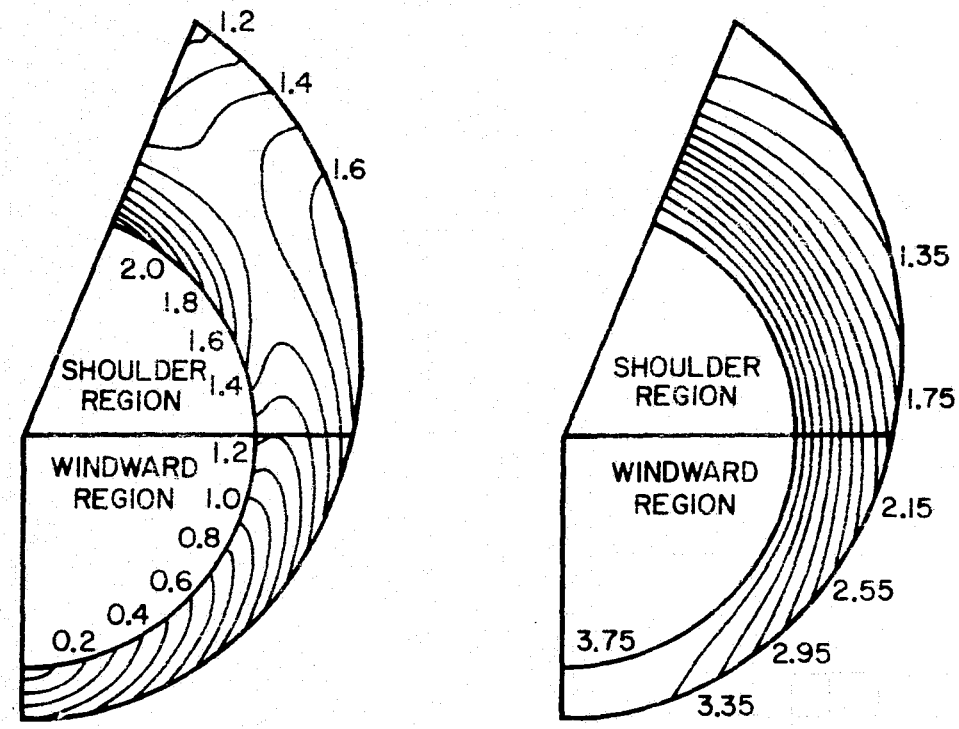

(a) CROSSFLOW MACH NUMBER, $M_{cf}=\left[\frac{v^2+w^2}{a^2}\right]^{1/2}$

(b) STREAMLINE PATTERN. ENTROPY PARAMETER, $S=\frac{p}{\rho^{\gamma}}$

Figure 10. Crossflow Mach number and entropy parameter contours in the windward and shoulder regions; $M_\infty = 7$, $\theta_c = 20°$, $\alpha = 30°$

crossflow sonic lines lies well upstream of the windward outflow boundary located at $\phi = 90°$.

The constant entropy contours in Figure 10b represent the streamline pattern. The shoulder region contours match precisely those obtained by the method of characteristics (13, 34).

Results for the leeward region flowfield are presented in Figure 11. The floating bow shock dips slightly in the leeward symmetry plane (Figure 11a). The shock shape thus represents the so-called "anomalous" position (23, 35) and differs from the "regular" position of the extrapolated bow shock.

The analysis presented in Reference 35 lends support to the floating-fitting solution for the bow shock shape. In Reference 35 an expression is derived, based on the assumption of small incidence, for the angle of attack at which the bow shock transitions from the regular to the anomalous position. For $M_\infty = 7$, $\theta_c = 20°$, and $\gamma = 1.4$ the maximum shock standoff distance moves out of the leeward symmetry plane when $\alpha > 4.1°$. The formation of the crossflow shock and the lift off of the vortical singularity at large angles of attack is not accounted for in this analysis. Results presented in Reference 54, however, do verify the change to the anomalous position for $\alpha = 5°$ and the movement of $\theta_{s_{max}}$ increasingly away from the symmetry plane for angles of attack up to 15°.

The density distribution behind the bow shock is shown in Figure 11b. The solution verifies the conjecture (13) that for relatively "thick" cones with "moderate" or large free-stream Mach numbers it might be expected that the bow shock will retain nonzero intensity in the leeward symmetry plane.

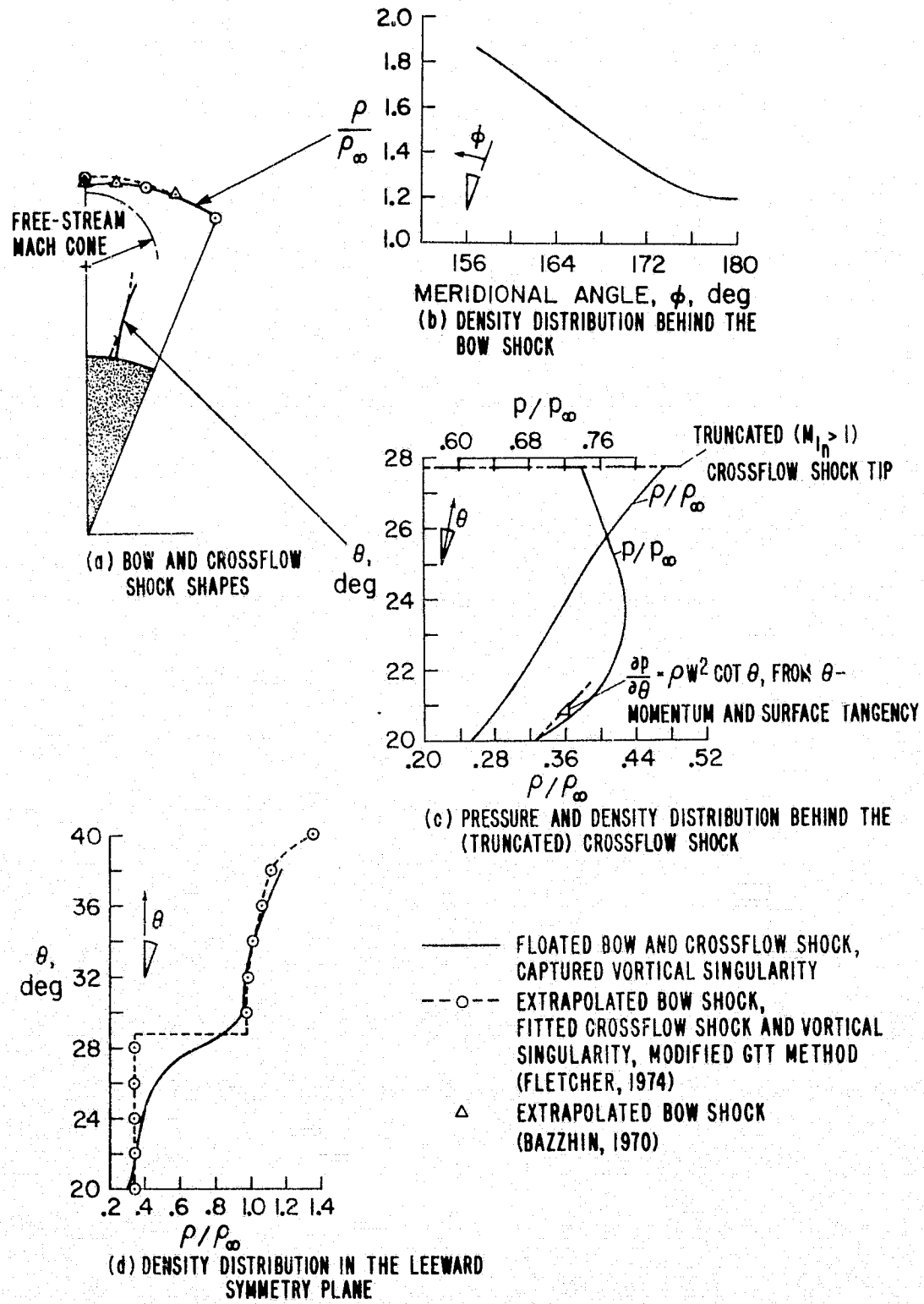

Figure 11. Leeward region solution; $M_\infty = 7$, $\theta_c = 20°$, $\alpha = 30°$

That is, although the bow shock dips in the leeward symmetry plane, it does not reach the free-stream Mach cone (Figure 11a). The density behind the bow shock in Figure 11b drops to about 1.2 times the free-stream value.

The crossflow shock, in Figure 11a, is perpendicular to the surface at its base. Away from the surface, the crossflow shock bends very slightly towards the crossflow upstream direction. The normal intersection of the crossflow shock with the cone surface is not imposed in the floating-fitting code, but evolves as the steady state conical solution is approached.

The length of the crossflow shock in Figure 11a is the length of the fitted portion only. As described in Chapter V, the fitting scheme is not applied all the way to the crossflow shock tip (where the upstream normal Mach number is one).

The pressure and density distributions on the downstream side of the crossflow shock are shown in Figure 11c. Tentative evidence for the presence of a conical logarithmic singularity, analogous to that found in two-dimensional flow, is provided by noting the difference between the Rankine-Hugoniot determined p_θ slope at the cone surface with that from the normal momentum equation with $v = 0$

$$p_\theta = \rho w^2 \cot\theta \qquad (\text{at} \quad \theta = \theta_c) \tag{76}$$

(plotted as a dashed line in Figure 11c).

This numerical evidence is, of course, only speculative. In lieu of an analytical proof, further numerical parametric studies are needed to support this conjecture on the existence of a logarithmic singularity.

The leeward symmetry plane density distribution, obtained by solving the conservation-law form of the governing equations without any special treatment of the vortical singularity, is compared with a modified GTT method solution (34) in Figure 11d. The strong density discontinuity at the vortical singularity is spread out over several θ-degrees in the singularity-captured solution. From the leeward symmetry plane density (and u-velocity) distributions it may be inferred that the singularity-captured solution demonstrates, at least qualitatively, lift off of the vortical singularity. However, the smearing out of the singularity, which closely resembles the viscous behavior observed experimentally, gives rise to the largest total enthalpy errors ($\sim O(1\%)$) in the flowfield (see Accuracy and Convergence Section of Chapter III). The θ-direction velocity component in the leeward symmetry plane (v-velocity) is negative at the bow shock, stagnates at the vortical singularity and again at the cone surface, and should be positive between the singularity and the surface. With a singularity-captured solution small oscillations in the v-velocity distribution between the singularity and the surface (where the magnitude of v is small) can cause negative v-velocities. Thus, some flow features near the singularity are not resolved using the singularity-capturing approach.

Implementation of the floating-fitting procedure for the vortical singularity, presented in Chapter V, does not improve the resolution of the singularity. The fitting technique requires accurate information from the flowfield interior (transmitted by the w_Y derivative) which is computed using the conservation-law dependent variables. However, large gradients in the flowfield, but not discontinuities, exist adjacent to the leeward

symmetry plane. Thus, unlike the flow regions on each side of floating-fitted shocks, the neighborhood of the singularity is not smooth, especially in the θ-direction. The conservation-law formulation tends to smooth these gradients. The floating-fitting scheme, in turn, moves the singularity and imposes jump conditions based on the smoothed interior flowfield values. The result of this complicated interplay between the singularity, the symmetry plane boundary conditions, and the flowfield interior is that a small vortical singularity velocity remains (nonconvergence) while the neighboring flowfield still resembles the singularity-captured solution. A new set of dependent variables for the flowfield interior, similar to those suggested in Reference 55, might help to resolve the singularity. However, the conservation-law form has proven to be very convenient in regards to the crossflow shock end-point treatment; such benefits would be lost with a change of dependent variables.

A symmetrical half-plane solution is presented in Figure 12. The bow shock loses its strength on the leeward side as it approaches tangency with the free-stream Mach cone (Figure 12a). The density behind the bow shock, plotted in Figure 12b, thus becomes equal to that of the free stream on the leeward side. Kentzer's shock boundary scheme accurately maintains the zero strength shock solution.

The floating-fitting result is in agreement with the conclusion in Reference 16 that for relatively "thin" cones or small free-stream Mach numbers the bow shock will degenerate into a Mach wave in the leeward symmetry plane.

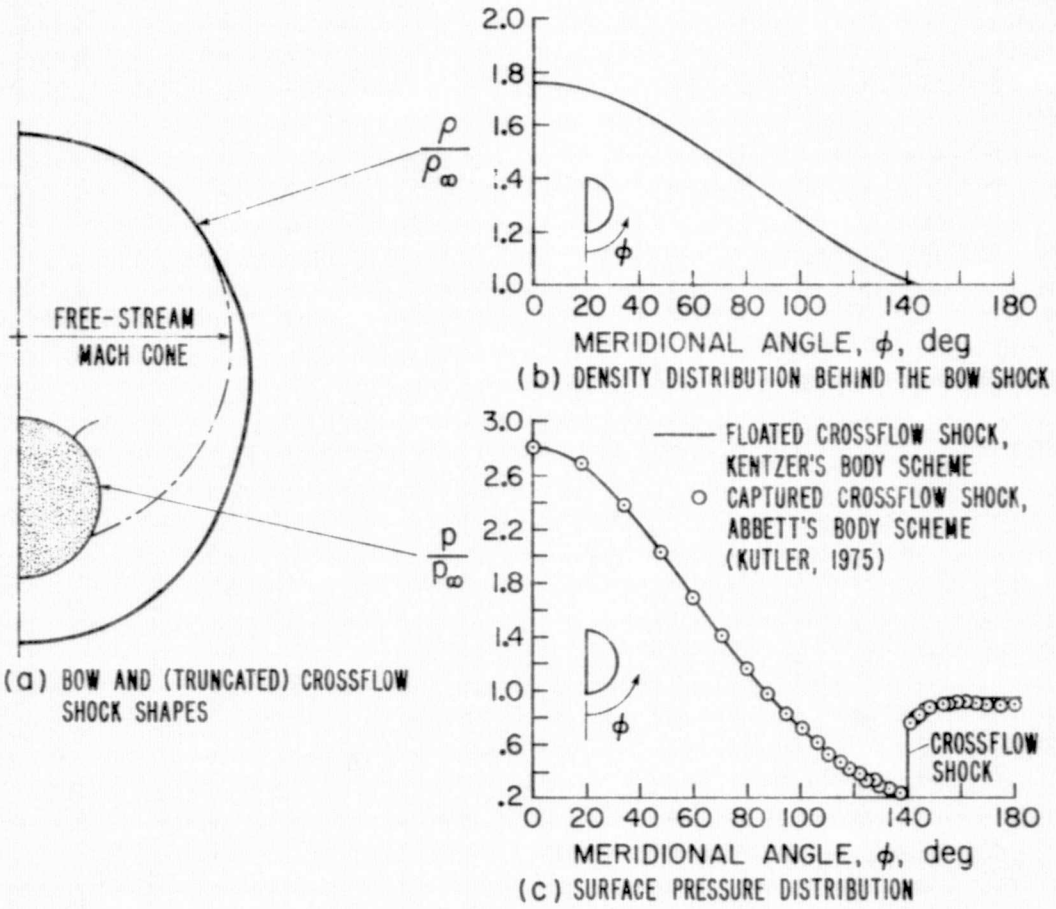

Figure 12. Symmetrical half-plane solution; $M_\infty = 3$, $\theta_c = 7.5°$, $\alpha = 15°$

As shown in Figure 12a, the crossflow shock (fitted portion) does not extend very far into the flowfield interior. The pressure jump across the crossflow shock is apparent in Figure 12c where the surface pressure distribution is shown. The floating-fitting results in Figure 12c match those obtained by a shock-capturing approach with slight differences occurring downstream of the crossflow shock. The captured internal shock appears as a sharp jump due to the alignment of the shock with the mesh, the clustering of points near shock, and its relatively weak strength.

CHAPTER VII. CONCLUDING REMARKS

Complicated flowfields occur about the geometrically simple circular cone at large angles of attack in a supersonic free stream. The cone problem serves as convenient test of numerical techniques intended for the computation of multidimensional flowfields containing embedded discontinuities. The conical nature of the problem provides a clear accuracy assessment that is not available in the calculation of flows about complex nonconical configurations.

All of the established numerical methods have encountered difficulties with cone at large angle of attack calculations. The most successful technique to date, a modification of the method of lines, is restricted to cases in which the crossflow sonic lines extend to the bow shock.

In this study an explicit finite-difference technique, based on the concept of floating-fitting discon inuities, has been described. Results have been presented which demonstrate the capability of the method over a range of Mach numbers, cone angles, and angles of attack. The technique has been shown to accurately compute both strong embedded shocks and vanishingly weak peripheral shocks. The method does not resolve the structure of the flowfield in the immediate vicinity of the vortical singularity.

From a pragmatic standpoint, the computer code for the floating-fitting algorithm, which must include logic for numerous discontinuity crossings of the computational mesh, is necessarily lengthy. However, the execution times are not excessive since most mesh points require no special treatment. The necessity to input several a priori estimates and generate initial con-

ditions coupled with the overall complexity of the code makes each case a trial and error process.

From a theoretical viewpoint, it is recommended that future efforts might be directed towards refining the shock tip calculation. Also, the treatment of the vortical singularity might benefit from a study of the mutual influence of boundary condition schemes with various sets of dependent variables in the flowfield interior.

ACKNOWLEDGMENTS

The authors thank Dr. Vijaya Shankar for his creative suggestions and acknowledge the financial support provided by NASA-Ames Research Center and the Engineering Research Institute at Iowa State University.

REFERENCES

1. Busemann, A. "Drücke auf Kegelförmige Spitzen bei Bewegung mit Überschallgeschwindigkeit." Zeitschrift für Angewandte Mathematik und Mechanik, 9, No. 6 (December 1929), 496 - 498.

2. Taylor, G. I., and Maccoll, J. W. "The Air Pressure on a Cone Moving at High Speeds." Proceedings of the Royal Society, 139, Series A, No. 838 (February 1933), 278 - 311.

3. Stone, A. H. "On Supersonic Flow Past a Slightly Yawing Cone." Journal of Mathematics and Physics, 27, Part I (April 1948), 67 - 81.

4. Kopal, Z. "Tables of Supersonic Flow Around Cones." Department of Electrical Engineering Tech. Report No. 1, Massachusetts Institute of Technology, 1947.

5. Ferri, A. "Supersonic Flow Around Circular Cones at Angles of Attack." NACA Technical Note 2236, November 1950.

6. Hayes, W. D., and Probstein, R. F. Hypersonic Flow Theory, Volume I, Inviscid Flows. 2nd ed., Applied Mathematics and Mechanics, Volume 5A. New York: Academic Press, 1966.

7. Klunker, E. B., South, J. C., and Davis, R. M. "Calculation of Nonlinear Conical Flows by the Method of Lines." NASA Technical Report TR R-374, October 1971.

8. Stocker, P. M., and Mauger, F. E. "Supersonic Flow Past Cones of General Cross-Section." Journal of Fluid Mechanics, 13, No. 3 (July 1962), 383 - 389.

9. Eastman, D. W., and Omar, M. E. "Flow Fields About Highly Yawed Cones by the Inverse Method." AIAA Journal, 3, No. 9 (September 1965), 1782 - 1784.

10. Ndefo, D. E. "Supersonic Flow Past a Yawed Cone Calculated by a Direct Method." Aero. Sciences Report No. AS-68-2, University of California, Berkeley, May 1968.

11. Ndefo, D. E. "A Numerical Method for Calculating Steady Unsymmetrical Supersonic Flow Past Cones." Aero. Sciences Report No. AS--68-11, University of California, Berkeley, May 1969.

12. Jones, D. J. "Numerical Solutions of the Flow Field for Conical Bodies in a Supersonic Stream." National Research Council of Canada Aeronautical Report LR-507, July 1968.

13. Bazzhin, A. P. "Some Results of Calculations of Flows Around Conical Bodies at Large Incidence Angles." Lecture Notes in Physics, Springer-Verlag, No. 8, Proceedings of the Second International Conference on Numerical Methods in Fluid Dynamics, Berkeley, California, September 15 - 19, 1970, 223 - 229.

14. Nakao, S. "Supersonic Flow Past Conical Bodies at Large Angles of Attack." Institue of Space and Aeronautical Science ISAS Report No. 534, University of Tokyo, November 1975.

15. Camarero, R. "A Reference-Plane Method for the Solution of Three-Dimensional Supersonic Flows." Aeronautical Quarterly, 27, Part 1 (February 1976), 75 - 86.

16. Gonidou, R. "Supersonic Flows Around Cones at Incidence." NASA Technical Translation TTF-11, 473, January 1968.

17. Babenko, K. I. "Investigation of Three-Dimensional Supersonic Gas Flow Around Conic Bodies." Proceedings of the Eleventh International Congress of Applied Mechanics, Munich, Germany, 1964, Springer-Verlag, 1966, 749 - 755.

18. Moretti, G. "Inviscid Flow Field Past a Pointed Cone at an Angle of Attack, Part I—Analysis." General Applied Sciences Laboratories Technical Report No. 577, December 1965.

19. Moretti, G., and Pandolfi, M. "Analysis of the Inviscid Flow About a Yawed Cone, Preliminary Studies." PIBAL Report No. 72-18, Polytechnic Institute of Brooklyn, May 1972.

20. Melnik, R. E. "Vortical Singularities in Conical Flow." AIAA Journal, 5, No. 4 (April 1967), 631 - 637.

21. Smith, J. H. B. "Remarks on the Structure of Conical Flow," in Progress in Aerospace Sciences, Vol. 12, pp. 241 - 272, Oxford: Pergamon Press, 1972.

22. Bakker, P. G., and Bannink, W. J. "Conical Stagnation Points in the Supersonic Flow Around Slender Circular Cones at Incidence." Department of Aeronautical Engineering Report VTH-184, Delft University of Technology, Delft, The Netherlands, November 1974.

23. Bachmanova, N. S., Lapygin, V. I., and Lipnitskii, Y. M. "Supersonic Flow Past Circular Cones at Large Angles of Attack." Fluid Dynamics, 8, No. 6 (May 1975), 915 - 919.

24. Fletcher, C. A. J. "Vortical Singularity Behind a Highly Yawed Cone." AIAA Journal, 13, No. 8 (August 1975), 1073 - 1078.

25. George, O. L. "An Experimental Investigation of the Flow Field Around an Inclined Sharp Cone in Hypersonic Flow." Sandia Laboratories Report SC-RR-69-577, September 1969.

26. Feldhuhn, R. H., Winkelmann, A. E., and Pasiuk, L. "An Experimental Investigation of the Flowfield Around a Yawed Cone." AIAA Journal, 9, No. 6 (June 1971), 1074 - 1081.

27. Houwink, R., and Nebbeling, C. "Experimental Investigation of the Leeward Flow Field of a Cone at High Incidence in Supersonic Flow." Delft Progress Report, Series C: Mechanical and Aeronautical Engineering and Shipbuilding, No. 1, 1975, 69 - 76.

28. Nebbeling, C., and Bannink, W. J. "Experimental Investigation of the Supersonic Flow Field About a Slender Cone at High Incidences." Department of Aerospace Engineering Report LR-233, Delft University of Technology, Delft, The Netherlands, November 1976.

29. Kutler, P., and Lomax, H. "The Computation of Supersonic Flow Fields About Wing-Body Combinations by 'Shock-Capturing' Finite Difference Techniques." Lecture Notes in Physics, Springer-Verlag, No. 8, Proceedings of the Second International Conference on Numerical Methods in Fluid Dynamics, Berkeley, California, September 15 - 19, 1970, 24 - 29.

30. Ivanov, M. Y., and Kraiko, A. M. "Calculation of the Supersonic Flow Around Conical Bodies." U.S.S.R. Computational Mathematics and Mathematical Physics, 13, No. 6 (January 1975), 228 - 245.

31. Kutler, P. "Computation of Three-Dimensional, Inviscid Supersonic Flows." Lecture Notes in Physics, Springer-Verlag, No. 41, Progress in Numerical Fluid Dynamics, 1975, 287 - 374.

32. Miyazawa, M. "A Numerical Analysis of Conical Flowfields." Proceedings of the 10th International Symposium on Space Technology and Science, Tokyo: AGNE Publishing, 1973, 433 - 442.

33. McRae, D. S. "A Numerical Study of Supersonic Viscous Cone Flow at High Angle of Attack." AIAA Paper 76-97, 1976.

34. Fletcher, C. A. J. "Supersonic Flow About Cones at Large Angles of Attack." College of Engineering Report No. FM-74-8, University of California, Berkeley, May 1974.

35. Zolotova, N. V. "On the Shape of the Shock in Nonsymmetric Hypersonic Flow Around a Circular Cone." Fluid Dynamics, 9, No. 1 (June 1975), 137 - 139.

36. Moretti, G. "Thoughts and Afterthoughts About Shock Computations." PIBAL Report No. 72-37, Polytechnic Institute of Brooklyn, December 1972.

37. Moretti, G. "Experiments in Multidimensional Floating Shock-Fitting." PIBAL Report No. 73-18, Polytechnic Institute of Brooklyn, August 1973.

38. Moretti, G. "Three-Dimensional, Supersonic, Steady Flows with any Number of Imbedded Shocks." AIAA Paper 74-10, 1974.

39. Moretti, G. "Floating Shock Fitting Technique for Imbedded Shocks in Unsteady Multidimensional Flows." Proceedings of the 1974 Heat Transfer and Fluid Mechanics Institute, Corvallis, Oregon, June 12 - 14, 184 - 201.

40. Moretti, G. "On the Matter of Shock Fitting." Lecture Notes in Physics, Springer-Verlag, No. 35, Proceedings of the Fourth International Conference on Numerical Methods in Fluid Dynamics, Boulder, Colorado, June 24 - 28, 1974, 287 - 292.

41. Moretti, G. "A Circumspect Exploration of a Difficult Feature of Multidimensional Imbedded Shocks." Proceedings of the AIAA 2nd Computational Fluid Dynamics Conference, Hartford, Connecticut, June 19 - 20, 1975, 10 - 16.

42. Salas, M. "The Anatomy of Floating Shock Fitting." Proceedings of the AIAA 2nd Computational Fluid Dynamics Conference, Hartford, Connecticut, June 19 - 20, 1975, 47 - 54.

43. Richtmyer, R. D. "Methods for (Generally Unsteady) Flows with Shocks: A Brief Survey." Lecture Notes in Physics, Springer-Verlag, No. 18, Proceedings of the Third International Conference on Numerical Methods in Fluid Mechanics, Paris, France, July 3 - 7, 1972, 72 - 81.

44. Nieuwland, G. Y., and Spee, B. M. "Transonic Airfoils: Recent Developments in Theory, Experiment, and Design." Annual Review of Fluid Mechanics, 5, 1973, 119 - 150.

45. Roache, P. "Recent Developments and Problem Areas in Computational Fluid Dynamics." Lecture Notes in Mathematics, Springer-Verlag, No. 461, Computational Mechanics, International Conference on Computational Methods in Nonlinear Mechanics, Austin, Texas, 1974, 195 - 256.

46. Cheng, S. I. "A Critical Review of Numerical Solution of Navier-Stokes Equations." Lecture Notes in Physics, Springer-Verlag, No. 41, Progress in Numerical Fluid Dynamics, 1975, 78 - 225.

47. Tracy, R. R. "Hypersonic Flow Over a Yawed Circular Cone." Graduate Aeronautical Laboratories Memorandum No. 69, California Institute of Technology, August 1963.

48. Thomas, P. D., Vinokur, M., Bastianon, R., and Conti, R. J. "Numerical Solution for the Three-Dimensional Hypersonic Flow Field of a Blunt Delta Body." AIAA Journal, 10, No. 7 (July 1972), 887 - 894.

49. MacCormack, R. W. "The Effect of Viscosity in Hypervelocity Impact Cratering." AIAA Paper 69-354, 1969.

50. Abbett, M. J. "Boundary Condition Computational Procedures for Inviscid Supersonic Steady Flow Field Calculations." Final Report No. 71-41, Aerotherm Corporation, 1971.

51. Davy, W. C., and Reinhardt, W. A. "Computation of Shuttle Nonequilibrium Flow Fields on a Parallel Processor." Aerodynamic Analyses Requiring Advanced Computers, Part II, NASA Special Publication SP-347, March 1975, 1351 - 1376.

52. Kentzer, C. P. "Discretization of Boundary Conditions on Moving Discontinuities." Lecture Notes in Physics, Springer-Verlag, No. 8, Proceedings of the Second International Conference on Numerical Methods in Fluid Dynamics, Berkeley, California, September 15 - 19, 1970, 108 - 113.

53. Rainbird, W. J. "Errors in Measurement of Mean Static Pressure of a Moving Fluid Due to Pressure Holes." National Research Council of Canada DME/NAE Quarterly Bulletin No. 1967 (3), 1967.

54. Fletcher, C. A. J., and Holt, M. "Supersonic Viscous Flow over Cones at Large Angles of Attack." Journal of Fluid Mechanics, 74, Part 3 (April 1976) 561 - 591.

55. Babenko, K. I., Voskresenskiy, G. P., Lyubimov, A. N., and Rusanov, V. V. "Three-Dimensional Flow of Ideal Gas Past Smooth Bodies." NASA Technical Translation TTF-380, 1966.

56. Pandolfi, M. "Supersonic Flow About Elliptic Cones with Large Semi-axis Ratios." Instituto di Macchine E Motori Per Aerombili Pubblicazione N. PP172, December 1975.

APPENDIX A. SHOULDER REGION CALCULATION

The shoulder region flowfield about highly inclined cones is most efficiently calculated by a two-dimensional meridional marching algorithm rather than a three-dimensional iterative relaxation approach. The procedure requires that the parameters M_∞, α, and θ_c are such that there exists a region of supersonic meridional velocity component extending from the cone surface to the bow shock (Figure 2a). The principle features of the technique are outlined below.

Dependent and Independent Variables

The steady Euler equations in cylindrical polar coordinates (z, r, ϕ) with the z-axis coincident with the cone centerline, r the cylindrical radial direction, and ϕ the meridional angle measured from the windward symmetry plane, may be written in weak conservation-law form as

$$E'_z + F'_r + G'_\phi + H' = 0 \tag{A1}$$

where E', F', G', and H' are the four-component vectors

$$E' = \begin{Bmatrix} \rho u \\ kp + \rho u^2 \\ \rho uv \\ \rho uw \end{Bmatrix}, \qquad F' = \begin{Bmatrix} \rho v \\ \rho uv \\ kp + \rho v^2 \\ \rho vw \end{Bmatrix},$$

$$G' = \frac{1}{r}\begin{Bmatrix} \rho w \\ \rho wu \\ \rho wv \\ kp + \rho w^2 \end{Bmatrix}, \qquad H' = \frac{1}{r}\begin{Bmatrix} \rho v \\ \rho uv \\ \rho (v^2 - w^2) \\ 2\rho vw \end{Bmatrix} \tag{A2}$$

The velocity components u, v, and w are in, respectively, the z, r, ϕ-directions. The pressure p and density ρ are nondimensionalized with respect to their free-stream stagnation values and the reference speed is

the maximum adiabatic speed. The constant k is related to the ratio of specific heats γ by

$$k = \frac{\gamma - 1}{2\gamma} \tag{A3}$$

The governing equations are made complete by the steady flow conservation of energy relation

$$p = \rho(1 - u^2 - v^2 - w^2) \tag{A4}$$

In order to treat the bow shock as an outer boundary of the computational domain, the independent variable transformation,

$$\left.\begin{aligned} \zeta &= z \\ \xi &= \frac{r - r_c(z)}{r_s(\phi, z) - r_c(z)} \\ \Phi &= \phi \end{aligned}\right\} \tag{A5}$$

where

$r_c = z \tan\theta_c \sim$ cone radius

$r_s(\phi, z) \sim$ bow shock radius

is applied to Equation (A1). With the assumption of conical flow, Equation (A5) represents a self-similar transformation and all flow derivatives with respect to ζ vanish. The transformed conical governing equations are

$$G^*_\Phi + F^*_\xi + H^* = 0 \tag{A6}$$

where

$$\left.\begin{aligned} G^* &= G' \\ F^* &= E'\xi_z + F'\xi_r + G'\xi_\phi \\ H^* &= H' - E'(\xi_z)_\xi - F'(\xi_r)_\xi - G'(\xi_\phi)_\xi \end{aligned}\right\} \tag{A7}$$

with

$$\left.\begin{aligned} \xi_z &= \frac{-r_{c_z} - \xi(r_{s_z} - r_{c_z})}{r_s - r_c} \\ \xi_r &= \frac{1}{r_s - r_c} \\ \xi_\phi &= \frac{-\xi\, r_{s_\phi}}{r_s - r_c} \\ (\xi_z)_\xi &= \frac{-r_{s_z} + r_{c_z}}{r_s - r_c} \\ (\xi_r)_\xi &= 0 \\ (\xi_\phi)_\xi &= \frac{-r_{s_\phi}}{r_s - r_c} \end{aligned}\right\} \tag{A8}$$

Finite-Difference Method

With initial conditions specified along a ϕ = constant line (provided by a windward region solution), MacCormack's predictor-corrector algorithm (Appendix B) is applied to Equation (A6) to advance the solution in the meridional direction. The calculation is terminated when the minimum Mach number in the hyperbolic marching direction falls below 1.05.

The F^*_ξ derivative at interior mesh points is approximated using the forward-predictor, backward-corrector version of MacCormack's algorithm. At the cone surface, F^*_ξ is always approximated by forward differences

(two-point) with all dependent variables being overwritten by the body boundary condition procedure following the corrector step. At the bow shock boundary, F^*_ξ is calculated using backward differences (two-point) in both the predictor and corrector steps. With given free-stream conditions, in conjunction with a sharp shock boundary procedure, information is transmitted across the bow shock only through the Rankine-Hugoniot relations. The shock boundary condition scheme is applied following both the predictor and corrector steps. The finite-difference value for pressure is accepted with the remaining flow variables being overwritten by the sharp shock procedure.

Stability Analysis

An estimate of a stable step size for the explicit MacCormack algorithm is provided by the C-F-L (Courant-Friedrichs-Lewy) condition

$$\Delta\Phi = \frac{(CN)\Delta\xi}{|\sigma_{max}|} \tag{A9}$$

where

$$|\sigma_{max}| = \frac{r}{\tilde{c}}\left\{\frac{|w(\tilde{a}u+v)+(w^2-a^2)(\tilde{b}/r)| + a\sqrt{(\tilde{a}u+v)^2+(w^2-a^2)(\tilde{a}^2+1)}}{w^2-a^2}\right\} \tag{A10}$$

represents the slope of a characteristic projected onto the ξ, Φ-plane with

$$\left.\begin{aligned}\tilde{a} &= \frac{\xi_z}{\xi_r}\\ \tilde{b} &= \frac{\xi_\phi}{\xi_r}\\ \tilde{c} &= \frac{1}{\xi_r}\end{aligned}\right\} \tag{A11}$$

and with the local speed of sound

$$a = \sqrt{\frac{k\gamma p}{\rho}} \tag{A12}$$

From linear theory, the Courant parameter CN should be less than or equal to 1.0; typically, for shoulder region calculations CN is set to 0.9.

Surface Boundary

Surface tangency, constant total enthalpy, and known surface entropy are imposed according to Abbett's (50) body boundary scheme.

Let a superscript (1) denote the surface flow values obtained from the finite-difference algorithm following the corrector step. In order for the velocity vector

$$\vec{q}^{(1)} = u^{(1)}\,\hat{i}_z + v^{(1)}\,\hat{i}_r + w^{(1)}\,\hat{i}_\phi \tag{A13}$$

to satisfy surface tangency, the flow is turned through a small isentropic compression or expansion where the turning angle is

$$\Delta\nu = \sin^{-1}\left(\frac{\vec{q}^{(1)} \cdot \hat{n}_c}{|\vec{q}^{(1)}|}\right) \tag{A14}$$

with

$$\hat{n}_c = \frac{-r_{c_z}\,\hat{i}_z + \hat{i}_r}{\sqrt{r_{c_z}^2 + 1}} \tag{A15}$$

the unit vector normal to the cone surface.

The series relations for the pressure following a turn through an oblique shock wave or an expansion through the small angle $\Delta\nu$ are

equivalent if terms $O(\Delta\nu^3)$ are neglected. With $\Delta\nu$ from Equation (A14) and the Mach number

$$M = M^{(1)} = \frac{q^{(1)}}{a^{(1)}} \tag{A16}$$

the pressure resulting from the tangency requirement is approximated by

$$p = p^{(1)} \left\{ 1 - \gamma M^2 \left[\frac{\Delta\nu}{\sqrt{M^2 - 1}} - \frac{(\gamma + 1)M^4 - 4(M^2 - 1)}{4(M^2 - 1)^2} \Delta\nu^2 \right] \right\} \tag{A17}$$

Since surface entropy is specified in the initial meridional plane and remains constant along the body streamline, the surface density follows from

$$\rho = \left(\frac{p}{S} \right)^{\frac{1}{\gamma}} \tag{A18}$$

The velocity modulus satisfying constant total enthalpy is obtained through the energy relation (Equation (A4))

$$q = \sqrt{1 - p/\rho} \tag{A19}$$

With the magnitude q and direction $\hat{t}_c$ known (where $\hat{t}_c$ denotes a unit vector tangent to the cone surface), the finite-difference velocity components $u^{(1)}$, $v^{(1)}$, and $w^{(1)}$ are replaced by

$$\left.\begin{aligned} u &= \frac{q}{|\vec{T}|} \left(u^{(1)} + N r_{c_z} \right) \\ v &= \frac{q}{|\vec{T}|} \left(v^{(1)} - N \right) \\ w &= \frac{q}{|\vec{T}|} w^{(1)} \end{aligned}\right\} \tag{A20}$$

where N is the scalar

$$N = \frac{\vec{q}^{(1)} \cdot \hat{n}_c}{\sqrt{r_{c_z}^2 + 1}}$$

$$= \frac{-u^{(1)} r_{c_z} + v^{(1)}}{r_{c_z}^2 + 1} \tag{A21}$$

and $\vec{T}$ the tangent vector

$$\vec{T} = \vec{q}^{(1)} - \left(\vec{q}^{(1)} \cdot \hat{n}_c\right)\hat{n}_c = |\vec{T}|\hat{t}_c$$

$$= \vec{q}^{(1)} - N\left(-r_{c_z}\hat{1}_z + \hat{1}_r\right) \tag{A22}$$

with magnitude

$$|\vec{T}| = \sqrt{\left(u^{(1)} + N r_{c_z}\right)^2 + \left(v^{(1)} - N\right)^2 + \left(w^{(1)}\right)^2} \tag{A23}$$

Shock Boundary

The two-dimensional shoulder region calculation is performed in the plane perpendicular to the cylindrical z-axis. Since the flowfield is self-similar, the slope of the bow shock in the z-direction is simply

$$r_{s_z} = \frac{r_s}{z} \tag{A24}$$

The slope of the bow shock in the marching meridional direction r_{s_ϕ} is obtained by inverting the relation for the component of the free-stream velocity normal to the bow shock $\tilde{u}_1$, where the subscript 1 refers to the bow shock upstream conditions. The resulting two roots are

$$r_{s_\phi} = r_s \left\{ w_1 \kappa \pm \tilde{u}_1 \sqrt{\kappa^2 + \frac{r_{s_z}^2 + 1}{w_1^2 - \tilde{u}_1^2}} \right\} \tag{A25}$$

where

$$\kappa = \frac{v_1 - u_1 r_{s_z}}{w_1^2 - \tilde{u}_1^2} \tag{A26}$$

with the free-stream velocity components

$$\left.\begin{aligned} u_1 &= q_1 \cos\alpha \\ v_1 &= -q_1 \sin\alpha \cos\phi \\ w_1 &= q_1 \sin\alpha \sin\phi \end{aligned}\right\} \tag{A27}$$

In Equation (A25) the appropriate root when $w_1^2 > \tilde{u}_1^2$ contains the + sign while the - sign is used if $w_1^2 < \tilde{u}_1^2$. The exact equality $w_1^2 = \tilde{u}_1^2$, which would lead to a zero in the denominator of κ, is not encountered numerically. In typical shoulder region calculations the switch in sign occurs without any difficulties at those meridional stations bounding the ϕ-location at which $w_1^2 = \tilde{u}_1^2$.

The bow shock computational plane boundary in the shoulder region code is computed following a "pressure approach" (48). With the known initial bow shock downstream pressure p_2 (where $p_2 = p_2^n$ prior to the predictor step and $p_2 = \overline{p_2^{n+1}}$ prior to the corrector step), the corresponding upstream normal velocity is given by the shock jump condition

$$\tilde{u}_1^2 = \frac{\gamma^2 - 1}{4\gamma} \frac{p_1}{\rho_1} \left[\frac{p_2}{p_1} + \frac{\gamma - 1}{\gamma + 1} \right] \tag{A28}$$

Substitution of $\tilde{u}_1$ into Equation (A25) gives the rate of change of the bow shock radius in the marching direction. The bow shock is advanced using the Euler predictor

$$\overline{r_s^{n+1}} = r_s^n + \Delta\phi\, r_{s_\phi}^n \tag{A29}$$

and modified Euler corrector

$$r_s^{n+1} = r_s^n + \frac{\Delta\phi}{2}\left[r_{s_\phi}^n + \overline{r_{s_\phi}^{n+1}}\right] \tag{A30}$$

sequence.

At the advanced ϕ-level the pressure behind the bow shock, obtained from the MacCormack algorithm with one-sided differencing in the ξ-direction, is the only flow variable accepted. The finite difference density result is discarded in favor of the Rankine-Hugoniot value

$$\rho_2 = \rho_1 \frac{\frac{p_2}{p_1} + \frac{\gamma - 1}{\gamma + 1}}{1 + \frac{\gamma - 1}{\gamma + 1}\left(\frac{p_2}{p_1}\right)} \tag{A31}$$

Equation (A28) gives the updated $\tilde{u}_1$ and Equation (A25) supplies the updated shock slope r_{s_ϕ}. Finally, the updated velocity components, computed from the shock jump relations applied at the updated shock position, are (the shock having been propagated by Equation (A29) or Equation (A30))

$$v_2 = v_1 + \frac{|\tilde{u}_1|\,(1 - \rho_1/\rho_2)}{\sqrt{r_{s_z}^2 + (r_{s_\phi}/r_s)^2}} \tag{A32}$$

$$u_2 = u_1 - r_{s_z}(v_2 - v_1) \tag{A33}$$

$$w_2 = w_1 - \frac{r_{s_\phi}}{r_s}(v_2 - v_1) \tag{A34}$$

APPENDIX B. INTEGRATION ALGORITHM

The gas dynamic equations written in nonconservation-law form as

$$d_\tau + [B_1]d_X + [B_2]d_Y + A_3 = 0 \tag{B1}$$

or cast in weak conservation-law form as

$$U_\tau + F_X + G_Y + H = 0 \tag{B2}$$

are integrated at each point of the finite-difference mesh by the explicit, two-step Euler predictor/modified Euler corrector sequence

Predictor:

$$\overline{f^{n+1}_{J,K}} = f^n + \Delta\tau\, f^n_\tau \tag{B3}$$

Corrector:

$$f^{n+1}_{J,K} = \frac{1}{2}\left[\overline{f^{n+1}} + f^n + \Delta\tau\, \overline{f^{n+1}_\tau}\right] \tag{B4}$$

where f represents either the d or U vector. The mesh point indices (J,K) for, respectively, the X- and Y-directions have been omitted from the right side of Equations (B3) and (B4). The superscripts n, $\overline{n+1}$, and $n+1$ refer to in order the current, predicted, and advanced time levels $(\tau^{n+1} = \tau^n + \Delta\tau)$.

The MacCormack (49) variant of the Lax-Wendroff method, in which spatial derivatives are approximated by equally spaced, two-point, one-sided differences of altering direction in the predictor and corrector stages, is used at all mesh points not lying on boundaries or neighboring (in time or space) discontinuities. The resulting noncentered algorithm is second-order in both time and space.

For all floating-fitting applications forward differencing in the predictor is followed by backward differencing in the corrector (several permutations of the differencing direction sequence were tested and found to yield substantially the same results for the windward region of the flowfield about a cone at large angle of attack).

To illustrate; the MacCormack algorithm applied to Equation (B2) to advance the point (J,K) to time leve τ^{n+1} approximates U_{τ}^{n} in Equation (B3) by

$$U_{\tau}^{n}{}_{J,K} = -\frac{1}{\Delta X}\left[F_{J+1} - F_{J}\right] - \frac{1}{\Delta Y}\left[G_{K+1} - G_{K}\right] - H \tag{B5}$$

and $\overline{U_{\tau}^{n+1}}$ in Equation (B4) by

$$\overline{U_{\tau}^{n+1}}{}_{J,K} = -\frac{1}{\Delta X}\left[F_{J} - F_{J-1}\right] - \frac{1}{\Delta Y}\left[G_{K} - G_{K-1}\right] - H \tag{B6}$$

where the nonvarying sub- and superscripts on the right sides of Equations (B5) and (B6) have been deleted.

On boundary points, where only one direction is available for forming differences in both the predictor and corrector stages, equally-spaced three-point approximations (which are consistent with the overall second-order of the scheme) are used.

In the presence of discontinuities the usual MacCormack algorithm is modified to prevent forming differences in time or space that would cross a discontinuity surface. Where required, unequally spaced one-sided spatial derivative approximations replace the approximations in Equations (B5) and (B6). These modifications to MacCormack's scheme, necessitated by a floating-fitting approach, are dealt with in Chapter III.

1. Report No.	2. Government Accession No.	3. Recipient's Catalog No.
NASA TM-73,259		

4. Title and Subtitle	5. Report Date
COMPUTATION OF THE INVISCID SUPERSONIC FLOW ABOUT CONES AT LARGE ANGLES OF ATTACK BY A FLOATING DISCONTINUITY APPROACH	6. Performing Organization Code

7. Author(s)	8. Performing Organization Report No.
James Daywitt,* Paul Kutler,* and Dale Anderson**	A-7104

9. Performing Organization Name and Address	10. Work Unit No.
*Ames Research Center, Moffett Field, Calif. 94035 **Iowa State University, Ames, Iowa 50011	506-26-31
	11. Contract or Grant No.
	Technical Memorandum

12. Sponsoring Agency Name and Address	13. Type of Report and Period Covered
National Aeronautics and Space Administration Washington, D. C. 20546	14. Sponsoring Agency Code

15. Supplementary Notes

16. Abstract

The technique of floating shock fitting is adapted to the computation of the inviscid flowfield about circular cones in a supersonic free stream at angles of attack that exceed the cone half-angle. In those regions in which the governing conical equations are mixed elliptic-hyperbolic, the fully hyperbolic form is obtained by the addition of the temporal derivative. The resulting equations are applicable over the complete range of free-stream Mach numbers, angles of attack and cone half-angles for which the bow shock is attached. An explicit finite-difference algorithm is used to obtain the solution by an unsteady relaxation approach. The bow shock, embedded cross-flow shock, and vortical singularity in the leeward symmetry plane are all treated as floating discontinuities in a fixed computational mesh. Where possible, the flowfield is partitioned into windward, shoulder, and leeward regions with each region computed separately to achieve maximum computational efficiency. In addition, an alternative shock fitting technique which treats the bow shock as a computational boundary is developed and compared with the floating-fitting approach. Several surface boundary condition schemes are also analyzed.

The floating-fitting method is shown to yield excellent results for the bow and embedded shocks, however, the solution in the leeward symmetry plane exhibits viscous-like effects and does not appear to resolve the flowfield in the immediate vicinity of the vortical singularity.

17 Key Words (Suggested by Author(s))	18. Distribution Statement
Floating shock fitting Computational fluid dynamics Conical supersonic flow	Unlimited STAR Category — 02

19. Security Classif. (of this report)	20. Security Classif. (of this page)	21. No. of Pages	22. Price*
Unclassified	Unclassified	96	$4.75

*For sale by the National Technical Information Service, Springfield, Virginia 22161